TU Delft

Delft University of Technology

Document Version
Final published version

Licence
CC BY

Citation (APA)
Slaifstein, D., Mouli, G. R. C., Ramirez-Elizondo, L., & Bauer, P. (2026). Ageing-aware energy management for residential multi-carrier energy systems. *Journal of Energy Storage*, *173*, Article 122889. https://doi.org/10.1016/j.est.2026.122889

Important note
To cite this publication, please use the final published version (if applicable).
Please check the document version above.

Copyright
In case the licence states “Dutch Copyright Act (Article 25fa)”, this publication was made available Green Open Access via the TU Delft Institutional Repository pursuant to Dutch Copyright Act (Article 25fa, the Taverne amendment). This provision does not affect copyright ownership.
Unless copyright is transferred by contract or statute, it remains with the copyright holder.

Sharing and reuse
Other than for strictly personal use, it is not permitted to download, forward or distribute the text or part of it, without the consent of the author(s) and/or copyright holder(s), unless the work is under an open content license such as Creative Commons.

Takedown policy
Please contact us and provide details if you believe this document breaches copyrights.
We will remove access to the work immediately and investigate your claim.

This work is downloaded from Delft University of Technology.

Journal of Energy Storage 173 (2026) 122889

Contents lists available at ScienceDirect

Journal of Energy Storage

journal homepage: www.elsevier.com/locate/est

Research papers

Ageing-aware energy management for residential multi-carrier energy systems

Darío Slaifstein *, Gautham Ram Chandra Mouli, Laura Ramirez-Elizondo, Pavol Bauer

DC Systems, Energy Conversion & Storage, Electrical Sustainable Energy Department, Delft University of Technology, Mekelweg 8, Delft, 2628, Zuid-Holland, Netherlands

ARTICLE INFO

Dataset link: https://github.com/DarioSlaifsteinSk/AgeRMCES

Keywords:
Energy management
Battery degradation
Multi-carrier energy system

ABSTRACT

In the context of building electrification, the operation of distributed energy resources integrating multiple energy carriers (electricity, heat, mobility) poses a significant challenge due to the nonlinear device dynamics, uncertainty, and computational issues. As such, energy management systems seek to decide the power dispatch in the best way possible. The objective is to minimize and balance operative costs (energy bills or asset degradation) with user requirements (mobility, heating, etc.). Current energy management uses empirical battery ageing models outside of their specific fitting conditions, resulting in inaccuracies and poor performance. Moreover, the link to thermal systems is also overlooked. This paper presents an ageing-aware nonlinear economic model predictive controller for electrified buildings that incorporates physics-based battery ageing models. The models distinguish between energy storage systems (chemistry, ageing state, etc.) and make explicit the trade-off between grid cost and battery degradation. The proposed algorithm can either cut down on grid costs or extend battery lifetime (electric vehicle or stationary battery packs). Additionally, substituting NMC cells with LFP chemistries optimizes grid performance during the summer, yielding a 10% grid cost reduction and a 20% decrease in degradation. Finally, the grid cost and degradation of the presented MPC when using aged batteries are improved with respect to the state of the art by 10% and 5% respectively, in periods with high solar generation and low thermal loads like summer.

1. Introduction

The decarbonization of the economy as a whole is a significant challenge for modern societies. In particular, the sustainable transformation of both the energy and transport sectors poses significant technical and cultural challenges [1]. Both transitions couple in the population's homes where electricity, mobility, or heat are needed. Thus, possible synergies between the three systems can be exploited to achieve the desired decarbonization, freedom, resiliency, and cost savings at the local or aggregated level [2]. The successful exploitation of such coupling thus needs to be carefully tailored and built into the design of modern multi-carrier energy systems [2–9]. This necessarily leads to advanced energy management systems (EMS) that schedule and control the distributed energy resources (DER) [6,9–12]. Thus, the EMS needs to handle uncertainty introduced by electric vehicles [13], solar generation and loads, as well as the battery degradation [14–18]. The main goal of this work is to address this last point.

To dispatch and operate residential MCES, the literature suggests Model Predictive Control (MPC) [6,12], stochastic optimization [19], reinforcement learning (RL) [6,7,9] and many others. Usually, the basis of such advanced systems is a day-ahead plan or dispatch that schedules the power of the assets along the day [4,10,11,20–22]. This planner is usually an optimization-based system that uses approximated deterministic forecasts of certain inputs to schedule the different assets. The decisions taken are then implemented and modified in real time. The optimization models have to model the representative aspects of the different assets of the energy system. This includes their power limits, dynamics, and operational constraints. The standard approach is to limit the models to simplified linear or quadratic forms, overlooking most technological particularities [2,6,9,23–27]. This nonlinearities can be the efficiency of a heat-pump, the voltage response of a battery or the heat losses of a building. In particular, when several energy storage systems are present, the EMS has to decide which storage system to use and when. In this regard, battery energy storage systems (ESS) are limited by their ageing [5,10,15–18,28] or their availability for mobility [5,13]. Current battery energy storage system (BESS) control decisions impact its remaining lifetime, thus, having a control-oriented predictive model that accurately reflects the cost of current decisions is key for optimal operation [29]. The bigger the bias between the

* Corresponding author.
E-mail address: d.a.slaifstein@tudelft.nl (D. Slaifstein).

https://doi.org/10.1016/j.est.2026.122889
Received 27 August 2025; Received in revised form 17 April 2026; Accepted 26 May 2026
Available online 12 June 2026
2352-152X/© 2026 The Authors. Published by Elsevier Ltd. This is an open access article under the CC BY license (http://creativecommons.org/licenses/by/4.0/).

Nomenclature

Optimization, Control & Dynamics

$\lambda_{\text{buy/sell},t}$	Day-ahead buy and sell prices.
$\mathbb{E}_W$	Expectation with respect to the exogenous process W
$\mathcal{D}_t^\pi = [t; t+H]$	Prediction horizon window at time t
$\mathcal{P}_{a,[t,t+H]}$	Power trajectory for system a over horizon $[t, t+H]$
$\mathcal{S}_{a,[t,t+H]}$	State trajectory for system a over horizon $[t, t+H]$
$\overline{_}, \underline{_}$	Maximum and minimum variable bounds.
π	policy
$\theta_{a,t}$	Model parameters for system a at time t
$\tilde{}$	Approximated/estimated variable/function.
ε_{SoC}	Penalty deviation from required departure SoC
$^+, ^-$	Positive and negative variable components.
$a \in \mathbb{A}$	Set of energy assets.
$b \in \{\text{BESS}, \text{EV}\} \subset a$	Battery storage asset index
$B_{a,t}$	Belief state for asset a at time t
C_{grid}	Cost of electricity from the grid
C_{loss}	Loss cost or penalty
p_{SoCDep}	Penalty term for SoC deviation
p_{TESS}	Soft-constraint penalty of TESS overcharge
$P_{a,t} \in \mathcal{P}$	Power setpoint for system a at time t
$S^M_{a,t}(\cdot)$	Transition function for asset a at time t
$S_{a,t} \in \mathcal{S}$	State of system a at time t
T, H	Simulation and optimization horizons.
$t, t', \Delta t$	Time index, time index within a policy π and timestep.
$w = [w_{\text{grid}}, w_{\text{loss}}, w_{\text{SoC}}, w_{\text{TESS}}]$	Objective function weights.
W_{t+1}	Exogenous information process at time $t+1$
$X^\pi_t(\cdot)$	Policy function at time t

Battery Performance Model

η_c	Coulombic efficiency
$\tilde{S}^M_{b,t}(\cdot)$	Battery transition model with performance and ageing
$d^M_{b,t}(\cdot)$	Battery ageing model
$N_{p,b}$	Number of parallel branches
$N_{s,b}$	Number of cells in series
$OCV_{b,t}$	Open-circuit voltage at time t
$p^M_{b,t}(\cdot)$	Battery performance model
$Q_{b,t}$	Battery capacity at time t
$S_{b,t} = [SoC, v_t]^T_{b,t}$	Battery state vector at time t
$SoC_{b,t}$	State of Charge of battery b at time t
$t_{0,b}$	Battery elapsed lifetime
$v_{t,b,t}$	Terminal voltage of battery b
$x_{b,t} = i_{b,t}$	Control cell current to the battery model at time t

Battery Degradation Model

$\delta_{\text{SEI},b,t}$	SEI layer thickness
$\eta_{k,b,t}$	SEI kinetic overpotential
$\varepsilon_{e,b,t}$	Electrolyte volume fraction
$i_{\text{AM},b,t}$	Active material loss current
$i_{\text{SEI},b,t}$	SEI side reaction current
$i_{\text{cal},b,t}$	Calendar degradation current
$i_{\text{cycle},b,t}$	Cyclic degradation current
$i_{\text{loss},b,t}$	Total degradation current
$OCV_{n,b,t}$	Open-circuit voltage of anode
SoH	State of Health of the battery
$z_{b,t}, z_{b,0\%}, z_{b,100\%}$	Lithium stoichiometry at time t, and limits at 0 and 100%

Electric Vehicle (EV) Model

$\gamma_{\text{EV},t}$	EV availability at time t (1 = parked, 0 = driving)
μ_{drive}	Mean of EV driving power distribution
σ^2_{drive}	Variance of EV driving power distribution
$P_{\text{EV},t}$	EV charger power at time t
$P_{\text{tot,EV},t}$	Total power associated with EV at time t
$P_{\text{drive,EV}}$	Power consumed while driving
SoC^*_{dep}	Required SoC at departure
$t_{\text{dep/arr}} \sim \mathcal{T}_{\text{dep/arr}}$	Departure and arrival time of the EV

optimization model and reality the less trustworthy are the decisions and predictions made.

On the other hand, the interaction of electricity and heat is becoming more relevant as heating electrification intensifies, and single-carrier optimization might lead to under performance and cost inefficiencies. When investigating MCES, Ceusters et al. [6,7] use first-order linear models for both BESS and thermal energy storage system (TESS), neglecting any differences between their dynamics. Similarly, Ye et al. [9] does not mention any difference between storage systems nor include EVs in their system. Alpizar-Castillo, et al. [30] focuses on thermal dynamics, only incorporating BESS with linear models, without including EVs. Other works only focus on the electrical carrier without including coupling electrical heating and storage [4,10,16,31]. These last works apply different battery models to describe their key variables, such as state-of-charge SoC, terminal voltage v_t, and state-of-health SoH. In this multi-carrier context, the optimization needs accurate cost functions and predictive models to decide in which carrier to store energy. If no dynamic distinction is made between ESS then the predicted operation will be far from reality leading to over investment on inefficient technologies. Thus, this work integrates electrical and thermal storage models together in the same optimization, but using different dynamic models to reflect their particular technologies accordingly.

Unfortunately, although physical ageing mechanisms have been studied and modelled [5,14,32–35], they have been partially incorporated into EMS design of residential MCES through empirical ageing models [5,10,20,23]. Battery-ageing models fall within two categories: empirical or physics-based (PB) [5,17,28]. The first are the most widely used in the literature due to their simplicity. They are obtained by performing long standardized calendar and cycling ageing tests [5,28]. Unfortunately, empirical degradation models only have interpolation capabilities, usually use non-linear equations, can only predict regular cycles (average C-rate, minimum SoC, etc.), are prone to overfitting,

Table 1
Summary of Literature Review.

Ref.	Application	Loads/Carriers			Flexibility				Battery modelling				
		Elec. load	Space heating	Nat.Gas	TESS	EV	BESS	Heat pump	Performance	Degradation	Dynamic profile	Cathode chemistry	Used and new cells
[6,7,41]	Energy Hub	✓	✓	✓	✓		✓	✓	Coulomb counting				
[10]	HEMS	✓	Flow-based			✓	✓		Coulomb counting	Empirical			
[2]	Energy Hub	✓	✓	✓	✓		✓		Coulomb counting				
[9]	HEMS	✓	✓	✓	✓		✓		Coulomb counting				
[24]	HEMS	✓	✓	✓	✓	✓	✓		Coulomb counting				
[27]	Energy Hub	✓				✓	✓		Coulomb counting	Empirical			
[26]	Energy Hub	✓	Flow-based	✓	✓		✓	✓	Coulomb counting	Empirical			
[39,42]	Utility scale						✓		PBROM		✓	*	*
[14]	Fast-charging					✓			PBROM		✓	*	*
[15]	Fast-charging					✓			ECM	PBROM	✓	*	✓
[16]	HEMS	✓					✓		PB ECM		✓	*	*
[31]	HEMS	✓					✓		PB ECM		✓	*	*
[43]	HEMS	✓					✓		ECM	Empirical			✓
[44]	Microgrid	✓					✓		Coulomb Counting	Empirical			
This work	HEMS	✓	✓		✓	✓	✓	✓	ECM	PBROM	✓	✓	✓

Note *: Capable, but no Case Study.

and are chemistry dependent [28,35,36]. On the other hand, PB models are built through first-principles and specialized tests to identify individual degradation mechanisms [28,32,34]. They have extrapolation features, can be expressed in the state-space form, account for several cathode chemistries, and represent dynamic profiles such as EVs, utility scale BESS or any irregular load. However, they are also nonlinear and, in general, non-convex [28,32–34,37]. The integration of PB ageing models into the operation of BESS has been recently studied at the battery management system (BMS) level for standalone and EV applications [14–16,38–40] usually through control-oriented physics-based reduced order model (PBROM). In the cited references, important cost savings were achieved either by preserving battery lifetime or by making an explicit trade-off between the grid costs and capacity fade, even when implementing optimization horizons of a day or less. To the author's best knowledge, their integration into applications where the BESS interacts with more assets, such as transmission grids, microgrids, industry, and in particular buildings, has not been extensively researched yet [29]. In this work, physics-based models unlock a new level of EMS intelligence: the ability to differentiate **unique battery chemistries** and **evolve alongside the cell's actual aging process**, ensuring optimal dispatch across the entire lifecycle of the multi-carrier system.

The most relevant works can be found in Table 1. In summary, current optimization-based approaches that do use PBROM to actively trade off between degradation and economic benefits are restricted to standalone battery systems [14,15,33,38–40,42]. When the battery is integrated with larger systems (solar photovoltaics (SPV), EV, microgrid, etc.), battery dynamics are usually simplified and empirical models are used in most literature, leading to inaccurate degradation predictions and under utilization [10,16,31,43,44]. None of the above references include the integration with a thermal carrier or multiple storage devices, and if they do, they do not include ageing models, [2,7,24,26,27].

This paper bridges the previously mentioned gaps by introducing an innovative economic MPC framework that integrates **ageing physics-based reduced-order models (PBROM)** directly into the EMS algorithm of multi-carrier systems. Current Energy Management Systems (EMS) for residential multi-carrier energy systems (MCES) often operate without a complete understanding of how their decisions impact the long-term health and lifetime of their storage assets. This integration fundamentally changes how the EMS operates, moving from a short-sighted, price-based optimization to a more holistic, ageing-aware strategy. Our approach enables the system to choose the optimal power dispatch of each storage system based on:

- The co-optimization of both **fast electrical storage** (BESS and EV) and **slower thermal storage (TESS)**, recognizing their distinct response times and efficiencies, through distinct terminal sets.
- The recognition of different **cathode chemistries** in lithium-ion batteries, leading to different power dispatches and grid costs.
- The exploitation of parameter differences between **new and used batteries**, ensuring that the operational plan remains accurate and effective throughout the entire lifespan of the battery storage units.
- The capacity to identify **dominant degradation mechanisms**, which provides the EMS with the critical information needed to make decisions that not only meet demand but also actively preserve the health of the batteries depending on their ageing state.

2. Modelling and optimal controller

Our EMS is an optimization-based secondary controller that minimizes energy cost and battery ageing. A schematic of the MCES and the EMS is presented in Fig. 1. The system is composed of SPV, BESS, EV, power electronic interface (PEI), heat pump (HP), solar thermal (ST), TESS, grid connection and loads. On the left, the EMS decides the power dispatch $P^*_{a,t}$ at $t \in \mathcal{D}_t$ where $\mathcal{D}_t = [0, T]$, passing it down to the MCES simulator. The MCES simulator feeds back the state measurements $S_{a,t}$ to continue with the loop.

The following section describes the EMS models, following the Universal Modeling Framework (UMF) by Powell [45]. For a given system size, the objective is to handle the operation cost, which is composed of three parts: the net cost of energy from the grid C_{grid}, the degradation cost of losing storage capacity C_{loss}, and a penalty for not charging the EV p_{SoCDep}. The grid cost and the degradation cost are cumulative objectives because the goal is to optimize them through time, while the penalty for not charging the EV to the desired SoC level is only a point reward at departure times t_{dep}. The sequential decision problem (SPD) is then:

$$\min_{P^*_{a,t}} \quad \mathbb{E}_W[C_{\text{grid}} + C_{\text{loss}} + p_{\text{SoCDep}}] \tag{1a}$$

$$\text{s.t.} \quad S_{a,t+1} = S^M_a(S_{a,t}, P^*_{a,t}, W_{t+1}|\theta_{a,t}) \tag{1b}$$

$$P^*_{a,t} = X^\pi_t(S_{a,t}) \in \mathcal{P} \qquad \forall a \in \mathbb{A},\ t \in \mathcal{D}_t \tag{1c}$$

$$S_{a,t} \in \mathcal{S} \qquad \forall a \in \mathbb{A},\ t \in \mathcal{D}_t \tag{1d}$$

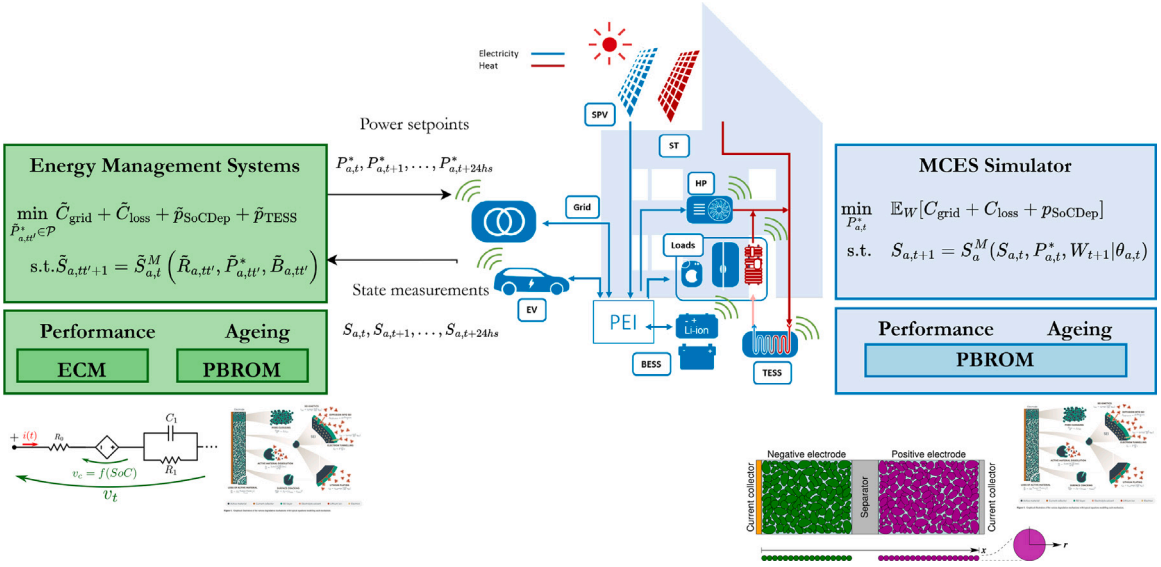

Fig. 1. Schematic diagram of the proposed electrified multi-carrier building.

with

$$\mathbb{A} = \{\text{SPV}, \text{grid}, \text{EV}, \text{BESS}, \text{HP}, \text{ST}, \text{TESS}\}\,. \tag{2}$$

where the components of the objective are:

$$C_{\text{grid}} = w_{\text{grid}} \sum_{t=0}^{T} \left(\lambda_{\text{buy},t}.P^+_{\text{grid},t} - \lambda_{\text{sell},t}.P^-_{\text{grid},t}\right).\Delta t \tag{3a}$$

$$C_{\text{loss}} = w_{\text{loss}}.c_{\text{loss}}.\sum_{t=0}^{T}\sum_{b} N_{s,b}.N_{p,b}.i_{\text{loss},b,t}.\Delta t,\ \forall\ b \in \{\text{BESS}, \text{EV}\} \subset a, \tag{3b}$$

$$p_{\text{SoCDep}} = w_{\text{SoC}}.\|\epsilon_{\text{SoC},t_{\text{dep}}}\|^2_2 \tag{3c}$$

where $S_{a,t}$ is the state vector, $P^*_{a,t}$ is the optimal decision for timestep t, W_{t+1} and is an exogenous process that introduces new information after making a decision. The mappings $S^M_{a,t}(.)$, and $X^\pi_t(.)$ are the transition function and optimal policy, respectively. The first is a set of equations describing the states and parameter evolution, and the second is the algorithm that finds the setpoints. The vector $\theta_{a,t}$ contains all the parameters of each asset a and changes over time t. The subindex $a \in \mathbb{A}$ corresponds to the assets shown in Fig. 1. The index b denotes the electric storage assets. The evaluation/simulation time window is $\mathcal{D}_t \in [0, T]$ and the timestep $\Delta t = 15$min. C_{loss} is explained in Section 3.3.2 and the penalty p_{SoCDep} in Section 3.4.

The following definitions of the elements are considered:

- The actions or decision variables are

$$P^*_{a,t} = [P_{\text{EV}}, P_{\text{BESS}}, P^{\text{e}}_{\text{HP}}]^T_t\,. \tag{4}$$

- The exogenous processes/inputs to the optimization W_{t+1} are the prices λ, EV availability γ, the solar power $P_{\text{PV/ST}}$, the electric and the thermal demands $P^{\text{e/th}}_{\text{load}}$:

$$W_{t+1} = [\lambda_{\text{buy/sell}}, \gamma_{n_{\text{EV}}}, P_{\text{PV}}, P_{\text{ST}}, P^{\text{e}}_{\text{load}}, P^{\text{th}}_{\text{load}}]^T_{t+1} \tag{5}$$

- The state vector has 2 components, the physical state of the system R_t, and beliefs about uncertain quantities or parameters B_t. All the observable physical quantities of our system, such as currents, voltages, and so on, are included in R_t. Finally, our belief state $B_{a,t}$ is composed of forecasts of W_{t+1}. These are defined as:

$$S_{a,t} = [R_a, B_a]^T_t \tag{6a}$$

$$B_{a,t} = [\tilde{\lambda}_{\text{buy/sell}}, \tilde{\gamma}_{\text{EV}}, \tilde{P}_{\text{PV}}, \tilde{P}_{\text{ST}}, \tilde{P}^{\text{e}}_{\text{load}}, \tilde{P}^{\text{th}}_{\text{load}}]^T_t \tag{6b}$$

- The superscripts e and th refer to electricity or thermal carriers. They are used when the subscript is the same.
- Both the actions and state vectors have upper and lower limits denoted as $\overline{P}^*_{a,t}$, $\underline{P}^*_{a,t}$, $\overline{S}_{a,t}$, and $\underline{S}_{a,t}$.
- All bidirectional powers, either actions or states, are modelled with their conversion efficiency η_a:

$$\eta_a S^+_{a,t} - \frac{1}{\eta_a} S^-_{a,t} = S_{a,t}\,, \tag{7}$$

  with $S^-_t \perp S^+_t$
- The order of the subscript is *"name, device, time index"*.
- Capital C denotes total cumulative cost in €, lowercase c denotes unit cost and lowercase w indicates tunning/scaling weight.

In Eq. (1) the planner or policy π wants to minimize the likelihood of the operational cost $\mathbb{E}[C]$ under the exogenous information process W. The problem at hand is a state-dependent problem in which our decisions $P^*_{a,t}$ are based on the current $S_{a,t}$, and influence future states $S_{a,t+1}$ (and thus, future decisions). Given the focus on future states and decisions, lookahead policies appear as attractive candidates for solving this SPD. Policy design and models are presented in the following Section 3.

3. Policy design

As mentioned before, the SPD in Eq. (1) is a state-dependent problem where current states influence future decisions. As such, Direct Lookahead (DLA) policies are commonly used in the literature to solve these problems. Two common examples of this policy family are optimal control strategies and stochastic dual dynamic programming. For this work, we focus on economic nonlinear MPC [46], which is a subset of optimal control where deterministic inputs (forecast medians in this case) are used to decide the actions for the incoming day. The process is shown in Fig. 2. The policy X^π takes inputs $\tilde{B}_{a,tt'}$ to decide the power dispatch $\tilde{P}^*_{a,tt'}$, optimizing over policy time $t' \in [t, t + H^{\text{DA/MPC}}]$ with $H^{\text{DA/MPC}}$ the optimization horizons.

More specifically, a DLA policy based on the devices' approximated dynamic models $\tilde{S}^M_t(\cdot)$. In this way, the EMS plans future actions based on approximate predictive models of devices. Approximation is denoted

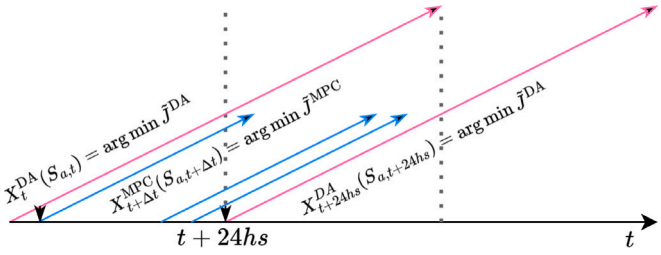

Fig. 2. Deterministic DLA policy with a day-ahead planner and economic MPC layer.

with˜. The policy is then solving the implicit economic Model Predictive Control (eMPC) given by:

$$\min_{\tilde{P}_{a,tt'}^{\mathrm{DA/MPC}} \in \mathcal{P}} \quad \tilde{J}^{\mathrm{DA/MPC}} \tag{8a}$$

$$\text{s.t.} \quad \tilde{S}_{a,tt'+1}^{\mathrm{DA/MPC}} = \tilde{S}_{a,t}^{M}\left(\tilde{R}_{a,tt'}^{\mathrm{DA/MPC}}, \tilde{P}_{a,tt'}^{\mathrm{DA/MPC}}, \tilde{B}_{a,tt'}^{\mathrm{DA/MPC}}\right) \tag{8b}$$

$$\tilde{S}_{a,tt'}^{\mathrm{DA/MPC}} \in S \qquad \forall a \in \mathbb{A} \tag{8c}$$

where:

$$\tilde{J}^{\mathrm{DA/MPC}} = \tilde{C}_{\mathrm{grid}}^{\mathrm{DA/MPC}} + \tilde{C}_{\mathrm{loss}}^{\mathrm{DA/MPC}} + \tilde{p}_{\mathrm{SoCDep}}^{\mathrm{DA/MPC}} + \tilde{p}_{\mathrm{TESS}}^{\mathrm{DA/MPC}} \tag{9a}$$

$$\tilde{p}_{\mathrm{TESS}}^{\mathrm{DA/MPC}} = w_{\mathrm{TESS}} \cdot \sum_{t'=t}^{H} \max\left(0, \tilde{SoC}_{\mathrm{TESS},tt'}^{\mathrm{DA/MPC}} - \overline{SoC}_{\mathrm{TESS}}\right) \Delta t \tag{9b}$$

In our policy, the upper limit constraint of the TESS, $\overline{SoC}_{\mathrm{TESS}}$, is implemented as a soft constraint to avoid infeasibilities during initialization or feedback. The penalty in the objective steers the $SoC_{\mathrm{TESS},t}$ towards the feasible region when the weight w_{TESS} is high enough. The eMPC is an adaptation of the policy presented in [47]. The only difference between the two layers (DA and MPC) is the length of the horizon and the terminal conditions, which will be analysed in Section 3.3.

The deterministic optimization problem in Eq. (8) approximates the real stochastic one by using forecasts, stored in $\tilde{B}_{a,tt'}$, and approximated models for the transition function $\tilde{S}_{a,t}^{M}$. In this model, the time t is the time at which the DLA policy is created and t' is the time inside the policy itself. Note the subtle difference between the approximated dynamics $\tilde{S}_{a,t}^{M}$ and the real ones $S_{a,t}^{M}$. This is not to be overlooked because the assumption that the predictions made by the policy π hold true can lead to disappointing results in real-world applications. Making these distinctions early in design reveals important insights for future stages. In this work, the energy management algorithm (EMA) has an approximated model $\tilde{S}_{a,t}^{M}$ to decide the setpoints $\tilde{P}_{a,tt'}^{*}$, to be implemented in a simulator $S_{a,t}^{M}$ containing detailed fidelity models. In the future, the simulator might as well grow enough to be considered a digital twin of the real building.

Thus the policy is:

$$X_t^{\mathrm{DA/MPC}}(S_{a,t}) = \arg\min_{P_{a,t}^{\mathrm{DA/MPC}}} \tilde{J}^{\mathrm{DA/MPC}} \tag{10}$$

subject to the approximate transition function $\tilde{S}_{a,t}^{M}$. This encompasses model approximation and forecasting ($\tilde{B}_{a,tt'}$) of the future inputs (W_{t+1}). The policy is then tuned by changing the weights w and implementing different NLP solver options (warm-starting, multi-start, etc.)

The approximate transition function $\tilde{S}_{a,t}^{M}(.)$ is the compendium of the equations specified in the rest of this section. In the remainder of this section, all equations will be presented just in terms of t for the sake of simplicity. However, the reader must remember that when inside the policy X^{π} they are defined under the policy's time t'.

3.1. Power & thermal balances

Assuming an indoor temperature setpoint decided either by the user or the thermal system [30,47,48], the building's thermal balance comes in as:

$$\tilde{P}_{\mathrm{ST},t} + P_{\mathrm{HP},t}^{\mathrm{th}} + P_{\mathrm{TESS},t} = \tilde{P}_{\mathrm{load},t}^{\mathrm{th}}\,. \tag{11}$$

The electric power balance, on the other hand, is:

$$\tilde{P}_{\mathrm{PV},t} + P_{\mathrm{BESS},t} + \gamma_{\mathrm{EV},t} \cdot P_{\mathrm{EV},t} + P_{\mathrm{grid},t} = \tilde{P}_{\mathrm{load},t}^{\mathrm{e}} + P_{\mathrm{HP},t}^{\mathrm{e}}\,. \tag{12}$$

where γ_{EV} is the EV availability, explained in Section 3.4.

3.2. Thermal modelling

The thermal assets are modelled in a linear way. The building has an air-to-water heat-pump that transforms electric power $P_{\mathrm{HP},t}^{\mathrm{e}}$ to heat-flow $P_{\mathrm{HP},t}^{\mathrm{th}}$ with a coefficient of performance η_{HP}:

$$P_{\mathrm{HP},t}^{\mathrm{th}} = \eta_{\mathrm{HP}} \cdot P_{\mathrm{HP},t}^{\mathrm{e}}\,, \tag{13}$$

where η_{HP} is assumed constant due to low variation of it during the year [30].

The thermal solar collector converts irradiance into heat, and assuming a constant linear relationship with the generated SPV power $P_{\mathrm{PV},t}$ as:

$$\tilde{P}_{\mathrm{ST},t} = \eta_{\mathrm{ST}} \cdot \tilde{P}_{\mathrm{PV},t}\,, \tag{14}$$

This work considers an underground, perfectly mixed water tank with independent charge and discharge coils as a TESS. Assuming no mass exchange between the TESS and the piping system the TESS the state of charge is:

$$SoC_{\mathrm{TESS},t+1} = SoC_{\mathrm{TESS},t} - \frac{\Delta t}{Q_{\mathrm{TESS}} \cdot 3600} \cdot \eta_{\mathrm{TESS}} \cdot P_{\mathrm{TESS},t}\,, \tag{15}$$

where η_{TESS} denotes the heat-exchanger efficiency, Q_{TESS} is the capacity in kWh. To avoid imposing an arbitrary periodicity on the TESS, no terminal conditions are used on its $SoC_{\mathrm{TESS},t}$. Thus, the TESS operates under its natural time constant.

3.3. Batteries

The remaining devices in the MCES are all battery-based ESS. Batteries have complex nonlinear dynamics, and several modelling techniques are presented in the literature [17]. In this work, models coming from empirical and physics-based approaches are used. The modelling is divided into two different sub-models: performance and ageing. Under the UMF, this is represented in the transition function $\tilde{S}_{b,t}^{M}(\tilde{S}_{b,t}, x_{b,t} | \theta_{b,t})$, which contains both the perf. model $p_{b,t}^{M}(.)$ and the ageing model $d_{b,t}^{M}(.)$. The performance model predicts stored energy $SoC_{b,t}$ and terminal voltage $v_{t,b,t}$. The ageing model is used to update the parameters of $p_{b,t}^{M}(.)$, as shown in Fig. 3. Even though the change in parameters $\theta_{b,t}$ becomes significant after considerable ageing has occurred, optimizing it in the short term can lead to considerable savings in the long and medium term [15,39,49,50]. This is because in PB ageing models, the relationship between ageing states and control actions is explicit, and the policy can directly minimize it through the internal states.

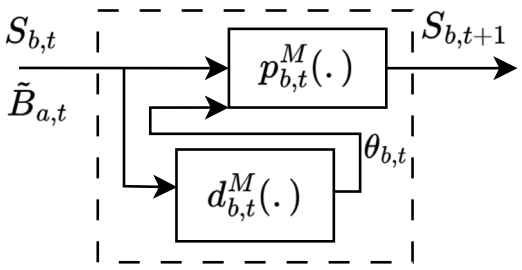

Fig. 3. Battery storage asset transition function diagram $\tilde{S}^M_{b,t}$.

The perf. model is then:

$$S_{b,t+1} = p^M_{b,t}\left(S_{b,t}, P_{b,t}, B_{a,t}|\theta_{b,t}\right) \tag{16}$$

where the components of the state depend on the functional form used for the model. In general, this is a nonlinear state space system.

The ageing model $d^M_{b,t}(.)$ is a set of equations that describes the dynamics of the performance parameters $\theta_{b,t}$.

$$\theta_{b,t+1} = d^M_{b,t}\left(S_{b,t}, P_{b,t}, B_{a,t}, \theta_{b,t}\right) \tag{17}$$

Finally, assuming that there is a strong daily usage pattern a terminal constraint is implemented to ease up feasibility and mitigate symmetries in the optimal control problem (OCP) of Eq. (8). Following [47], the daily periodical constraint in the first optimization of the day (X^{DA}_t in Fig. 2) is:

$$\tilde{SoC}^{\text{DA}}_{\text{BESS},tt'_1} = \tilde{SoC}^{\text{DA}}_{\text{BESS},tt'_1+24hs} \tag{18}$$

and in all other steps X^{MPC}_t the periodic condition is:

$$\tilde{SoC}^{\text{MPC}}_{\text{BESS},tt'_0} = \tilde{SoC}^{\text{MPC}}_{\text{BESS},tt'_0+H^{\text{MPC}}} \tag{19}$$

where $t_0 \le t_1 \le H \le T$. This way, the OCP is better computationally conditioned, but the planner still has the freedom to decide the state-of-charge at the beginning of each day ($SoC_{\text{BESS,24hs}}$). The proposed terminal condition has two key properties: it is more flexible than fixing $SoC_{\text{BESS,24hs}} = 50\%$, and it bounds the value function V_H of the OCP. Ideally, no terminal condition would be used to freely use all 3 storage systems. Unfortunately, to solve such an unbounded OCP, an optimization horizon H much larger than 48 h would be required [46,51].

3.3.1. Performance models $p^M_{b,t}$

For the performance submodel, two alternatives have been implemented: a simple Coulomb counting or bucket model (BM) and a first-order equivalent circuit model (ECM). A basic BM of the operation of a battery assumes that its output voltage v_t is linear with the state of charge SoC, assuming no internal resistance, and no-diffusion dynamics. Hence, the only equations of this model are:

$$SoC_{b,t+1} = SoC_{b,t} - \frac{\Delta t}{Q_{b,t}.3600}.\eta_c.i_{b,t}\,, \tag{20a}$$

$$i_{b,t} = \frac{P_{b,t}}{v_{t,b,t}.N_{s,b}.N_{p,b}}\,, \tag{20b}$$

$$OCV_{b,t} = a_{OCV,b} + b_{OCV,b}.SoC_{b,t}\,, \tag{20c}$$

$$v_{t,b,t} = OCV_{b,t}\,, \tag{20d}$$

$$S_{b,t} = [SoC_b, v_{t,b}, i_b]^T_t \tag{20e}$$

where $i_{b,t}$ is the current passing through the cell, $OCV_{b,t}$ is the open circuit voltage, η_c is the Coulombic efficiency [18], and $Q_{b,t}$ is the cell capacity in Ah. Each battery pack is assumed to be organized as a series connected module (SCM) where $N_{s/p,\,b}$ are the series cells per branch and parallel branches, respectively. In this model, the most relevant parameter in θ_b is the Q_b.

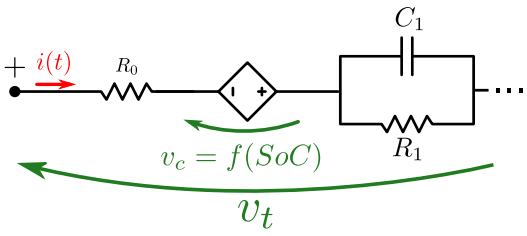

Fig. 4. First-order Equivalent Circuit Model.

A first-order ECM has improved accuracy due to the incorporation of diffusion and series resistance, as in Fig. 4. The performance sub-model $p^M_{b,t}(.)$ is then modified by adding the equation:

$$i_{R_1,b,t+1} = e^{-\frac{\Delta t}{R_{1,b}.C_{1,b}}}.i_{R_1,b,t} + \left(1 - e^{-\frac{\Delta t}{R_{1,b}.C_{1,b}}}\right).i_{b,t} \tag{21}$$

and modifying Eq. (20d) as in:

$$v_{t,b,t} = OCV_{b,t} - i_{R_1,b,t}.R_{1,b} - i_{b,t}.R_{0,b}\,, \tag{22}$$

where $i_{R_1,b,t}$ is the current flowing through R_1 in Fig. 4. Eqs. (20a)–(20c) are maintained. The ECM incorporates the series voltage drop that limits power output and the first-order diffusion dynamics. Here, the relevant parameters are $\theta = [Q, R_0]^T$ that usually define the cell's state of health SoH.

3.3.2. Degradation models $d^M_{b,t}(.)$

For the ageing models, the first alternative is an empirical sub-model presented by [35]. The empirical sub-model reduces all the degradation mechanisms into calendar and cyclic ageing.

$$i_{\text{cycle},b,t} = \frac{c_1.c_3}{c_4}.e^{c_2.|i_{b,t}|}.(1 - SoC_{b,t}).|i_{b,t}|\,, \tag{23a}$$

$$i_{\text{cal},b,t} = c_5.e^{-\frac{24\ \text{kJ}}{RT}}.\sqrt{t_{0,b} + t}\,, \tag{23b}$$

$$i_{\text{loss},b,t} = i_{\text{cycle},b,t} + i_{\text{cal},b,t}\,, \tag{23c}$$

and

$$Q_{b,t+1} = Q_{b,t} - \frac{\Delta t}{3600}.i_{\text{loss},b,t}\,. \tag{24}$$

where the fitting parameters $c_{1,\ldots,5}$ are taken from [10,35,52] and $t_{0,b}$ is the elapsed lifetime of the battery b.

For the physics-based alternative, the reduced order model (PBROM) from [15] is used. It accounts for two degradation mechanisms: the solid electrolyte interface (SEI) and active material loss (AM). The author also presents a PBROM for Li-plating, but given the low C-rate and standard temperature range of this application, it will not be included.

The growth of the SEI layer is modelled with a general reaction that aims to average all the different byproducts that compose the SEI layer. This is synthesized in the reversible SEI current i_{SEI}:

$$i_{\text{SEI},b,t} = \frac{k_{\text{SEI},b}.e^{\frac{-E_{\text{SEI},b}}{RT}}}{n_{\text{SEI}}.(1 + \lambda_b.\beta_b).\sqrt{t_{0,b} + t}} \tag{25}$$

where $k_{\text{SEI},b}$ is the kinetic rate of the average reaction, $E_{\text{SEI},b}$ is the activation energy of the reaction, n_{SEI} is the average number of e^- transferred through the layer, and λ_b and β_b are parameters depending on other variables such as $\eta_{k,b}$, $OCV_{n,b}$, z_b and others.

The system is completed with:

$$\eta_{k,b,t} = \frac{2.R.T}{F}.\sinh^{-1}\left(\frac{i_{b,t}}{n_{\text{SEI}}.a_s.A.L_n.i_0}\right) \tag{26a}$$

$$z_{b,t} = SoC_{b,t}.(z_{100\%,b} - z_{0\%}) + z_{0\%,b} \tag{26b}$$

$$\beta_b = e^{\frac{n_{\text{SEI}}.F}{R.T}.(\eta_{k,b} + OCV_{n,b,t} - OCV_{s,b})} \tag{26c}$$

where η_k is the SEI side reaction kinetic overpotential, z is the Li stochiometry of the cell, OCV_n is the open-circuit voltage of the anode made with an empirical fit, $OCV_s = 0.4V$ is the side reaction open-circuit voltage, and T is the cell temperature. It is assumed that the temperature T is constant over time and is controlled by the local primary control system of the BESS and EV. The rest of the parameters can be found in the Appendix A.

The loss of active material due to the mechanical stress of the electrode is modelled with:

$$i_{\text{AM},b,t} = k_{\text{AM},b}.e^{\frac{-E_{\text{AM},b}}{R.T}}.SoC_{b,t}.|i_{b,t}|.Q_{b,0} \tag{27}$$

The total ageing is the contribution of both mechanisms SEI layer growth and AM loss. The capacity fade current is:

$$i_{\text{loss},b,t} = i_{\text{SEI},b,t} + i_{\text{AM},b,t} \tag{28}$$

which is later used again in (24).

Now, by carefully inspecting Eq. (22), the reader will notice that if $R_{0,b,t}$ is incorporated as a variable in the OCP, Eq. (8), this would add another non-convex constraint to it (since $i_{b,t}$ can be either positive or negative). Thus, its evolution is only included in the simulator $S^M_{a,t}(.)$ updating the parameters without the policy X^π_t being directly aware of the process.

To model the power fade (i.e., the increase of R_0), the SEI layer thickness $\delta_{\text{SEI},b,t}$ growth is described by:

$$\delta_{\text{SEI},b,t+1} = \delta_{\text{SEI},b,t} + \frac{\Delta t}{M_{\text{SEI}}.n_{\text{SEI}}.F.\rho_{\text{SEI}}.A_n} i_{\text{SEI},b,t} \tag{29}$$

Hence, the dynamics of the series resistance R_0 are:

$$R_{0,b,t+1} = R_{0,b,t} + \frac{\varepsilon_s}{\kappa_{eff}}.\frac{\Delta t}{M_{\text{SEI}}.n_{\text{SEI}}.F.\rho_{\text{SEI}}.A_n} i_{\text{SEI},b,t} \tag{30}$$

The solvent S leaves the electrolyte to form the SEI layer; thus, the volume fraction of S evolves with:

$$\varepsilon_{e,b,t+1} = \varepsilon_{e,b,t} - a_s.\frac{\Delta t}{M_{\text{SEI}}.n_{\text{SEI}}.F.\rho_{\text{SEI}}.A_n} i_{\text{SEI},\ b,\ t} \tag{31}$$

3.4. Electric vehicle

From the point of view of a residential building, the EVs are a BESS with availability constraints and certain requirements regarding their SoC at departure time t_{dep}. For the availability γ, the probability distributions of departure (t_{dep}) and arrival (t_{arr}) times can be described as random variables $t_{\text{dep/arr}} \sim \mathcal{T}_{\text{dep/arr}}$, whose distributions $\mathcal{T}_{\text{dep/arr}}$ are taken from Elaad [53]. The availability γ_t will then be:

$$\gamma_t = \begin{cases} 0 & t \in [t_{\text{dep}};\ t_{\text{arr}}] \\ 1 & \text{otherwise} \end{cases}. \tag{32}$$

The power balance of an EV is

$$P_{\text{tot,EV},t} = \gamma_{\text{EV},t}.P_{\text{EV},t} + (1 - \gamma_{\text{EV},t})P_{\text{drive,EV}} \tag{33}$$

where $P_{\text{tot,EV},t}$ is the total power of the EV, $P_{\text{EV},t}$ is the charger power, and $P_{\text{drive,EV}}$ is the power consumed driving, assuming no public charging. The total power $P_{\text{tot,EV},t}$ is then used in Eq. (20b) and later for calculating the ageing of the EV batteries. The average driving power is also sampled from a Gaussian distribution $P_{\text{drive,EV}} \sim \mathcal{N}(\mu_{\text{drive}}, \sigma^2_{\text{drive}})$. This is because the EV battery pack degradation during driving needs to be accounted for in the operation strategy (charging and driving).

At t_{dep} the EV is required to be delivered at SoC^*_{dep}:

$$SoC_{\text{EV}}(t_{\text{dep}}) = SoC^*_{\text{dep}} \tag{34}$$

This is implemented as a penalty in the objective function, Eq. (8), as in any typical OCP. The deviation from the reference at the desired time is penalized with:

$$\varepsilon_{\text{SoC},t_{\text{dep}}} = SoC_{\text{EV}}(t_{\text{dep}}) - SoC^*_{\text{dep}} \tag{35}$$

Algorithm 1 MCES simulation.

1: **Define setpoint** $P_{a,t}$
2: **Define exogenous information** W_{t+1}
3: Recalculate $P_{\text{TESS},t}$ and $P_{\text{grid},t}$ using Eqs. (11) & (12), with $P_{a,t}$, and W_{t+1}
4: Simulate $SoC_{\text{TESS},t}$ using Eq. (15)
5: Simulate b performance using $p^M_b(.)$ PBROM [54]
6: Simulate b degradation using $d^M_{b,t}(.)$ PBROM [15]
7: Feed-back $S_{a,t}$ to the planner

Summing up, the three different storage systems have three different ways of handling their terminal set and value function bounds. The BESS has a periodic conditions Eqs. (18) and (19), which is a flexible alternative to the classic terminal daily periodicity. The EV follows a soft-tracking problem at t_{dep}. The TESS has no terminal condition. This flexible design is the key contribution to integrating all the storage systems and the non-convex PB models to the eMPC of Eq. (8).

4. MCES simulator $S^M_{a,t}(.)$

The simulator evaluates the policy π and closes the loop with the state measurements. It is designed to:

- Provide high-accuracy simulation results that act as plant measurements.
- Adjust/reject setpoints that violate hard constraints.
- Re-balance power in case of rejections or infeasible optimizations.

The whole process is defined in Algorithm 1. First, the power setpoints must be adjusted for the grid and TESS because the forecast used in X^π_t will never be the same as the actual exogenous inputs. Take a look at the balances, Eq. (11) and (12), which contain the loads and solar generation. It is clear that $\tilde{P} \neq P$ and a device must compensate for that difference. Thus, the simulator $S^M_{a,t}$ recalculates:

$$P_{\text{TESS},t} = P^{\text{th}}_{\text{load},t} - P_{\text{ST},t} - P^{\text{th}}_{\text{HP},t}\,. \tag{36}$$

$$P_{\text{grid},t} = P^{\text{e}}_{\text{load},t} + P^{\text{e}}_{\text{HP},t} - P_{\text{PV},t} - P_{\text{BESS},t} - \gamma_{\text{EV},t}.P_{\text{EV},t}\,. \tag{37}$$

Second, once these powers have been adjusted, the simulator uses these powers to obtain the true/actual/fidelity state $S_{a,t}$. For the TESS it recalculates Eq. (15). For the b, it uses LiiBRA.jl [54] to swiftly simulate PBROMs of the performance of the battery [17,55]. After that, the models from Jin [15] are used to calculate the true degradation outcome of the decisions $P^*_{a,t}$. Again, the reader must remember that the capacity fade (decrease in $Q_{b,t}$) is modelled in both the simulator $S^M_{a,t}$ and the approximate model of the planner $\tilde{S}^M_{a,t}$, whereas the power fade (increase in $R_{0,b,t}$) is only addressed in the simulator $S^M_{a,t}$. Finally, if an action $P^*_{b,t}$ causes a future state to go out of bounds ($S_{b,t+1} \leq \underline{S}_b$ or $S_{b,t+1} \geq \overline{S}_b$), the action is rejected and modified leaving b on the bound (either $\overline{S}_b$ or $\underline{S}_b$) until the next t. Finally, the carriers are rebalanced if necessary.

The final state $S_{a,t}$ is then fed back to the optimization-based controller. For practical implementation, in which the simulator is, in fact, an experimental setup, an online state observer is necessary to feed back the states to the EMS. This is particularly important for the ESS [17,18,56,57].

Despite the inherent inaccuracies of the simplified models used within the EMS planners $\tilde{S}^M_{a,t}(\cdot)$, the informed $SoH_{b,t}$ remains accurate due to the high-fidelity feedback provided by $S^M_{b,t}(\cdot)$. It is assumed that the primary control of the storage b will maintain the current spikes within tight bounds, avoiding any consequent voltage deviations within the sampling time $\Delta t = 15$min of the EMS. Thus, since the simulator

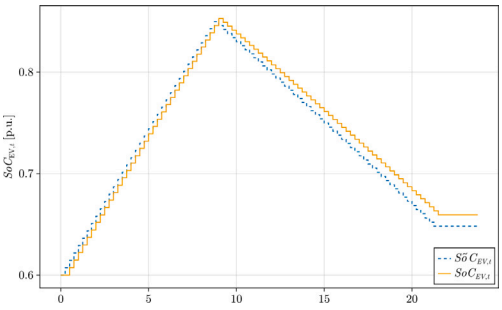

(a) Simulated and predicted SoC for the EV for $T = 24$hs and open-loop simulation.

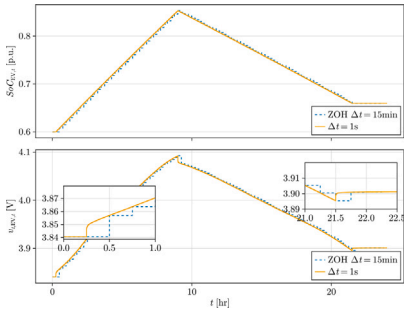

(b) Full simulation and reported down sampled state.

Fig. 5.

$S^M_{b,t}(\cdot)$ operates at a $\Delta t_s = 1$s resolution, the informed degradation captures the true physical response of the battery, including peak state values. These are later down-sampled to the $\Delta t = 15$min resolution of the planner X^π. The process effectively reduces the planner's error to a mere 15-minute communication lag (Fig. 5) and a zero-order-hold approximation. By utilizing the realized trajectories of $SoC_{b,t}$ and $v_{t,b,t}$ from the fidelity simulator $S^M_{a,t}(\cdot)$ rather than the planner's internal estimates, the system ensures that the reported capacity fade and degradation states reflect the actual operational stress on the battery, regardless of the planner's complexity.

5. Case studies

The building has a grid connection with a smart meter with 15 min resolution. The grid power P_{grid} is included in the state vector $S_{a,t}$. The system is composed of a 4 kWp SPV, a 15.6 kWh/12.5 kW BESS with nickel manganese cobalt oxides (NMC) or Lithium iron phosphate (LFP) cells, one 55.6 kWh/12.5 kW EV charging points, a 4 kWe heat pump, a 2.7 kWth solar thermal collector, a 200 kWh TESS, a 2.5 kWp electrical load, a 1.5 kWp thermal demand, and 17 kW LV grid connection. Power consumption profiles ($P^{\text{e}}_{\text{load}}$) were constructed for a year using data from 2021 to 2023 from TU Delft's Green Village smart meter data [58]. The output of the SPV is taken from [59,60], the market prices λ are taken from the EPEX day-ahead auction, and $\lambda_{\text{buy}} = 0.95\lambda_{\text{sell}}$ [61], and the heat demand $P^{\text{th}}_{\text{load}}$ was modelled as [30].

Algorithm 2 Rolling horizon algorithm.

Initialize hyperparameters t_0, Δt, $H^{\text{DA/MPC}}$, w, n_d
Initialize device states and inputs $S_{a,0}$
for $d \in 1 : n_d$ **do**
  Solve the day-ahead policy X^{DA_t} and obtain schedule $\mathcal{P}^{\text{DA}}_{a,[t,H^{\text{DA}}]}$.
  for $t \in 0 : H^{\text{MPC}}$ **do**
    Solve the deterministic continuous time policy X^{MPC_t} and obtain action $P^{\text{MPC}}_{a,t}$.
    Simulate $S_{a,t+1} = S^M_{a,t}(S_{a,t}, P^{\text{MPC}}_{a,t}, W_{t+1})$
    Update forecasts in $B^{\text{MPC}}_{a,tt'}$
    Move time window $t \leftarrow t + \Delta t^{\text{MPC}}$;
  end for
end for

Table 2
Summary of battery models in each controller.

Battery model	Scheduler BNoDeg	CEmpDeg	CPBDeg	Simulator PBROM
Performance	Bucket model Eq. 21	ECM Eq. 21–23	ECM Eq. 21–23	SPM PBROM [54]
Ageing	–	Empirical Eq. 24–25 [35]	PBROM Eq. 25–29 [15]	PBROM Eq. 25–29 [15]
Feature				
Dynamic Profile	Only performance.	ECM ✓ Emp. Deg ✗	✓	✓
Cathode Chemistry	No distinction	Only NMC	✓	✓
Used and New cells	Used cells are only smaller cells.	✓	✓	✓

The cells used are SANYO NCR18650 cells for NMC as in [15] and A123 cells for LFP [34]. Their datasets were taken from `PyBaMM` [62] and `LiiBRA` [54]. The ECMs for both cell types were fitted from synthetic cells simulated in `PyBaMM`, following the methodology in [17]. Once the simulated profiles are ready, the ECM parameters can be identified using subspace system identification as in [63]. The parameters can be found in Appendix A, Tables A.7 and A.8 along with a more detailed explanation of the identification pipeline. The capacity fade cost is assumed to be $c_{\text{loss}} = 1.2$ €/Ah, roughly 280-310€/kWh, depending on the average voltage.

The simulations were modelled and run using `Julia` [64], `JuMP` [65], and `InfiniteOpt` [66]. The chosen solver was KNITRO from Artelys [67]. All simulations were run using an Intel CPU at 2.60 GHz, 4 processors, and 32 GB of RAM. The base library for building and simulating EMS policies is open-source and free to use in `EMSmodule` [47] and the specific code to reproduce the following case studies can be found in the dataset link. Since this is a non-linear non-convex OCP, global optimality cannot be generally guaranteed [46,68]. Having this in mind, the implementation of the EMS approaches this limitation by: (i) using warm-starts as initial guess to ensure convergence to the same local optima, (ii) using the KNITRO tuner and multi-start in each individual step to increase the chance of finding the best local optima [67].

5.1. Case study I: Degradation model comparison

To test and validate our EMA the closed-loop control was simulated for two standard months (summer and winter) using 2023 data from the previously mentioned sources. Both are presented in Fig. 6. To quantify the impact of each performance and ageing model 3 eMPC controllers, 2 benchmarks and our proposed approach, were implemented:

- (*BNoDeg*) Including a bucket model and no degradation $w_{\text{loss}} = 0$, with $\tilde{S}^{M1}_{a,t}$ in Eq. (8).
- (*CEmpDeg*) Including a first-order ECM and empirical ageing for the b, with $\tilde{S}^{M2}_{a,t}$ in Eq. (8).
- (*CPBDeg*) Including first-order ECM with PBROM ageing for the b, with $\tilde{S}^{M3}_{a,t}$ in Eq. (8).

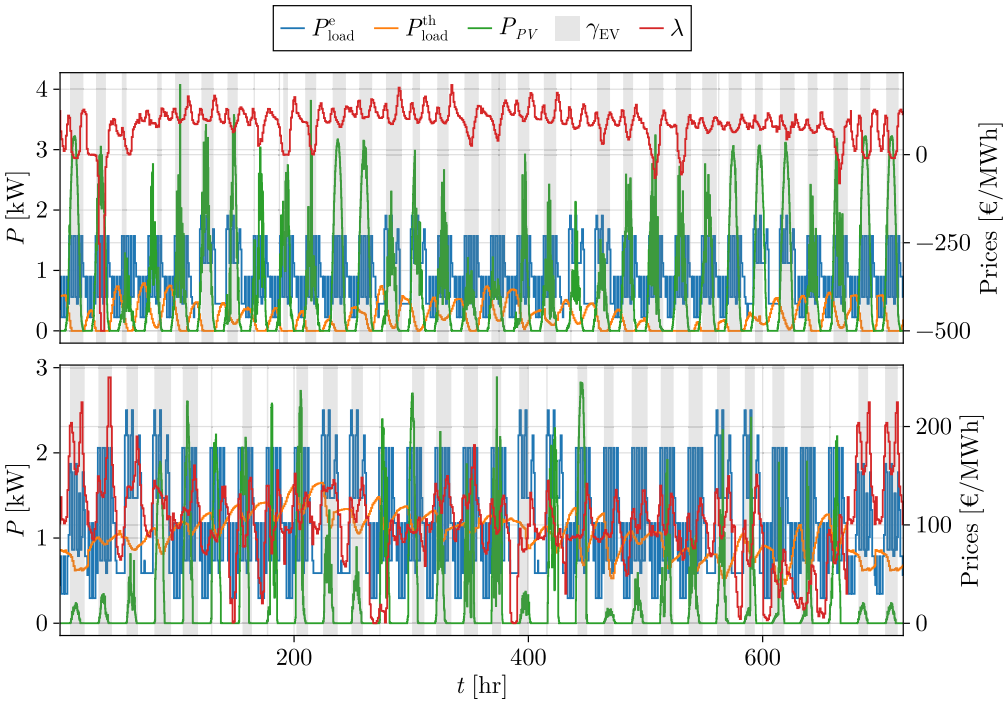

Fig. 6. Exogenous information W_{t+1}. Grey bands represent periods were the EV is not connected.

A summary of the key Eqs. and features of each of the planners can be found in Table 2. The simulation workflow is presented in Algorithm 2 and depicted in Fig. 2. First, the hyperparameters are initialized. This includes the time window to be optimized $D^{\pi}_{t} = [t; t + H]$, the number of days n_d, user preferences, the initial state $S_{a,0}$, and weights w. In our case $n_d = 29$, the weights are $w_{\text{grid}} = 1$, $w_{\text{loss}} = 0.01$ and $w_{\text{SoCDep}} = w_{\text{TESS}} = 1000$, since the first two represent real economic costs and the second represent penalties. At timestep t, the OCP in Eq. (8), is solved, obtaining the action $P^{*}_{a,t}$. Together with the exogenous information W_{t+1} the actions are passed to the simulator $S^{M}_{a,t}$ to get the feedback state $S_{a,t}$.

As a representative example, Fig. 7 presents the results for the proposed *CPBDeg* controller for a monthly period. It has the resulting power balances (electrical and thermal) and the use of the hybrid energy storage system (HESS). The electric ESS have daily cycles to minimize operating costs (energy arbitrage). This is particularly important for the EV since its mobility demand already establishes a daily periodicity. Thus, due to the EV's battery pack size and its natural periodicity, it becomes the main electric storage of the system. This frees up the BESS for energy arbitrage, trying to capture price variations when possible within the power balance. Thus, price volatility incentivizes cycling. However, due to the SEI model, batteries are also pushed downwards to the minimum ageing state at $\underline{SoC}_{b,t}$. Hence, the dispatch contemplates a trade-off between the 2 parts of the objective C_{grid} and Q_{loss}. On the thermal carrier, the $P^{\text{th}}_{\text{load},t}$ represents the heat losses of the building which have to be compensated by either ST, HP or TESS. In the summer, the losses during solar hours are almost zero and thus the ST charges the TESS. If the prices are negative enough then HP charges the TESS during $\lambda_t \leq 0$. In the winter, the TESS is charged with the HP early in the day when prices are low or during solar hours, in that order of priority, to later deliver heat to the demand at high price hours. In summary, during the summer price volatility is high with several hours with $\lambda_t \leq 0$, the EMS buys this energy to reduce costs. In winter, prices are less volatile and the load is higher, leading to fewer opportunities for arbitrage and overall higher costs.

The schedules of the HESS under the different controllers are summarized in Figs. 8–10. In the BESS, Fig. 8, the *BNoDeg* and *CPBDeg* cycle the battery pack more often. This is because *BNoDeg* does not contemplate ageing, and the *CPBDeg* equations relate minimizing Q_{loss} to $\underline{SoC}$. The *CEmpDeg* controller cycles less frequently, due to its overestimation of Q_{loss}, concentrating the operation around $\overline{SoC}$ to reduce the ageing of the BESS. This happens both in summer (top) and winter (bottom). Moreover, on many days the price variations are not large enough to afford ageing the BESS, thus *CPBDeg* chooses to maintain the SoC close to its lower bound. The two highlighted days are days where the *CPBDeg* outperforms the benchmarks and the BESS prioritizes C_{grid} over Q_{loss}.

For the EV timeseries comparison, Fig. 9, the user's mobility requirement leads to similar timeseries for all the planners. As expected, *BNoDeg* prioritizes short-term revenues and has the most frequent V2G, followed by *CPBDeg* and with *CEmpDeg* usually choosing the highest $SoC_{\text{EV},t}$ of the three. Again, this reflects the dependency of the empirical model, Eq. (23), with DoD. V2G mode suits the *CPBDeg* because it incentivizes discharging the EV, minimizing its degradation. This counterintuitive result is because the ageing PBROM shows how Q_{loss} is minimized by $\underline{SoC}$. Since p_{SoCDep} requires high SoC^{*}_{dep}, the dynamic combination of them both results in more V2G.

On the thermal side, presented in Fig. 10, the natural periodicity of the carrier is longer due to its thermal efficiencies, size and C-rate. Qualitatively, all three planners take similar decisions independent of the battery model used. This is because the TESS has a roundtrip efficiency η lower than the EV and BESS, and thus a longer optimization window H is needed for the TESS to show its flexibility value relative to the BESS or EV [51,69]. During the first week the initial $SoC_{\text{TESS},0}$ influences costs greatly. After the first week, the EMS has already steered the buffer to its desired setpoint. This means a high $SoC_{\text{TESS},t}$ during summer (high heat generation, low load) and a low setpoint during winter (low heat generation, high load). The high setpoint during summer entails 2 risks: overcharging the TESS (i.e., activating soft-constraint and curtailing ST) and not capturing negative prices due to past short-sightedness (TESS starting a day with a high SoC). Even though in the summer *CPBDeg* has the smallest ST curtailment the ageing models have a low overal impact. In other words, integrating ageing models does not change the overall TESS decisions, since the advanced cell models do not change the fact that $\eta_b \geq \eta_{\text{TESS}}$ and a bigger H is needed for the TESS to present valuable flexibility.

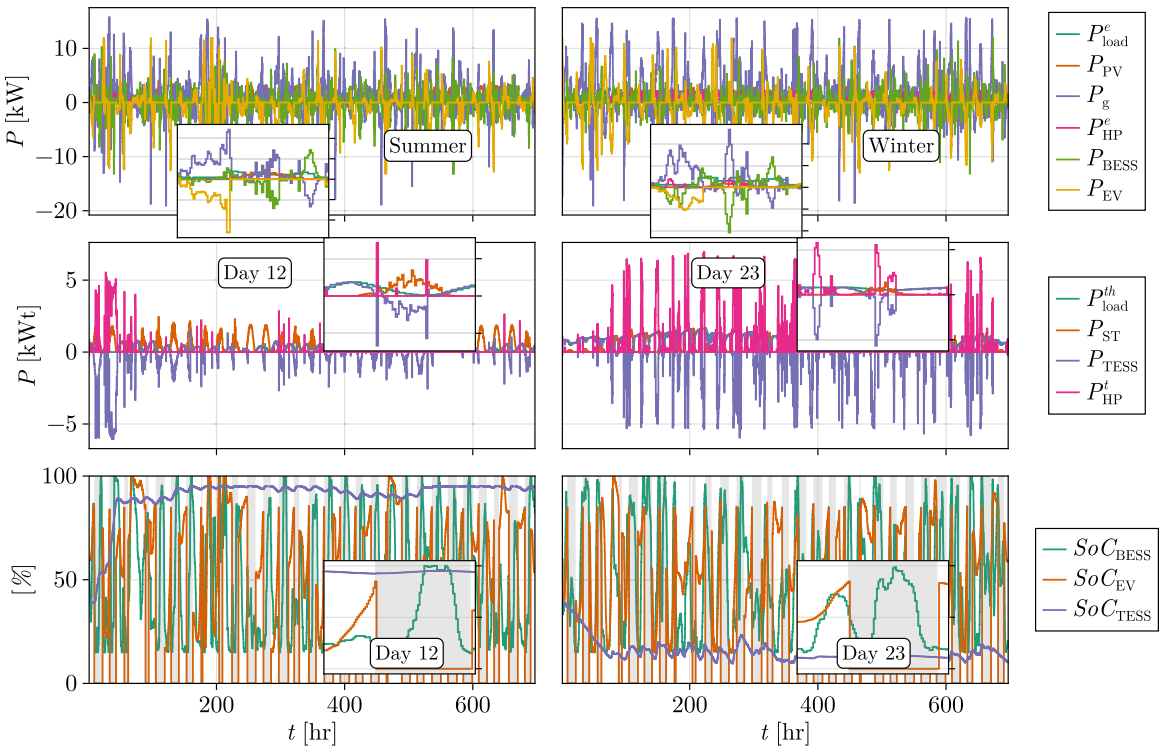

Fig. 7. Monthly dispatch of MCES under *CPBDeg* controller with $w_{loss} = 0.01$ for summer (left) and winter (right).

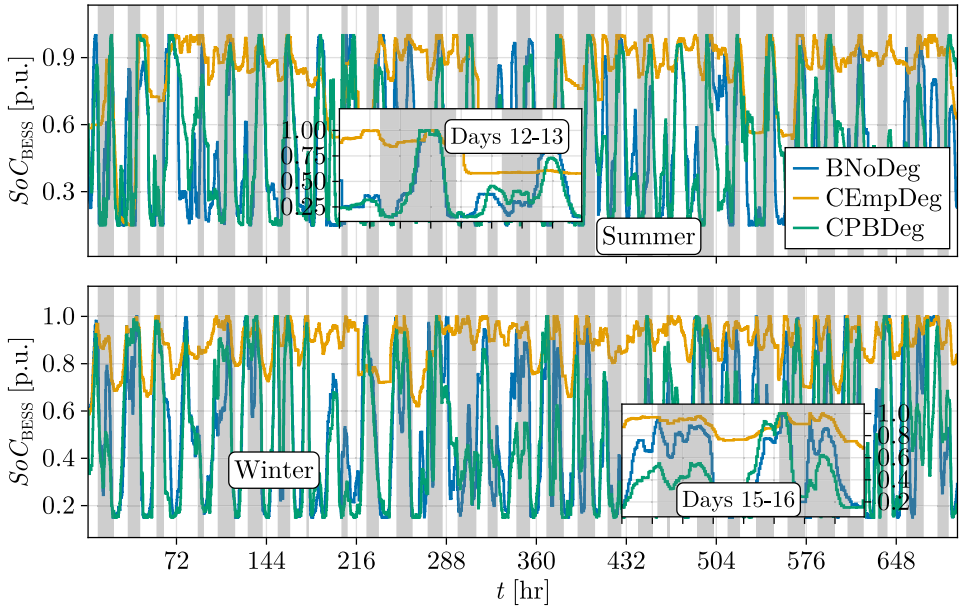

Fig. 8. Monthly simulation SoC_{BESS} for summer (top) and winter (bottom).

In summary, each storage system follows a distinct use represented in its terminal set. The EV follows a soft-tracking penalty p_{SoCDep}, the BESS follows a flexible daily periodicity, and the TESS handles medium-term thermal demand. Without the design of the mixed terminal set, the non-convex NLP would not converge to feasible locally optimal points, and thus is a key contribution of this paper.

The performance of each planner is summarized in Table 3. Starting with the grid cost C_{grid}, the best performer is the *BNoDeg* in the summer and winter. The worst performer is *CEmpDeg* and the PB controller *CPBDeg* stands in the middle. For the total capacity fade Q_{loss}, *CEmpDeg* has the lowest degradation while the *BNoDeg* has the highest. The

Table 3
Planner comparison cost summary with weights $w_{grid} = 1$, $w_{loss} = 0.01$, $w_{SoC} = w_{TESS} = 1000$.

Planner	C_g [€]		Q_{loss} [mAh]	
	summer	winter	summer	winter
BNoDeg	55.4	101.7	377.3	400.1
CEmpDeg	62.3	115.3	234.0	250.8
CPBDeg	57.6	109.9	343.2	351.7

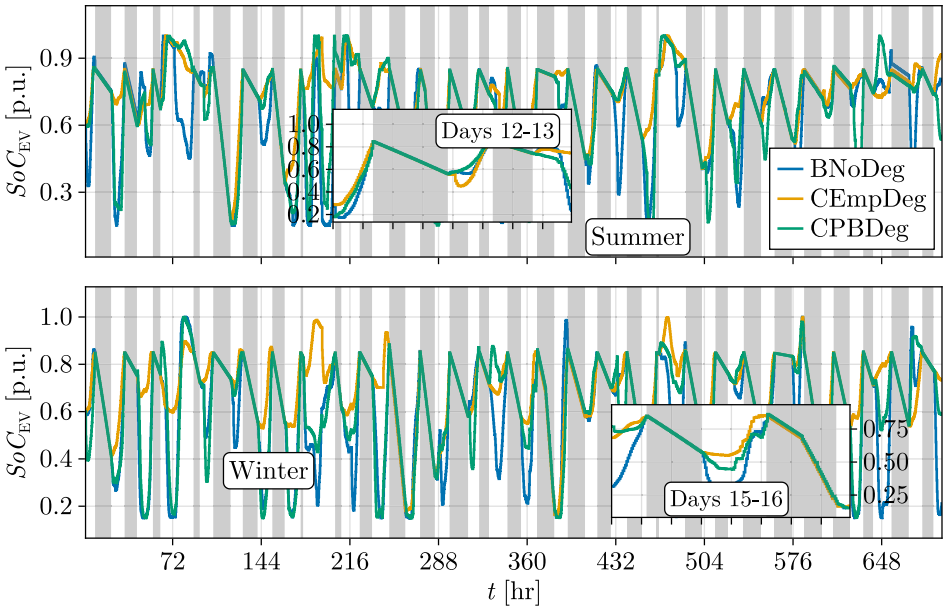

Fig. 9. Monthly simulation SoC_{EV} for summer (top) and winter (bottom). Grey bands indicate driving periods.

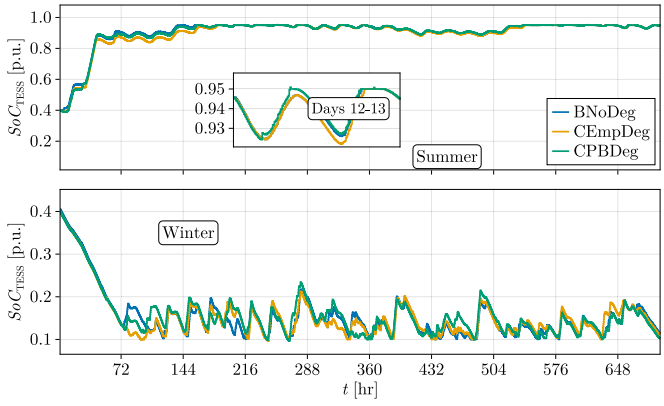

Fig. 10. Monthly simulation SoC_{TESS} for summer (top) and winter (bottom).

proposed ageing-aware *CPBDeg* has -10% less degradation than the *BNoDeg*, maintaining a reasonable C_{grid}.

However, just reviewing the objective function $J^{DA/MPC}$ is not enough. To dive deeper into the total storage usage, a quantitative analysis of the number of cycles done by the b is necessary. Fig. 11 presents the full equivalent cycles FEC over time t, showing that the *BNoDeg* controller has the most FEC, followed by *CPBDeg* and with the empirical controller *CEmpDeg* having the least throughput. When analysing the capacity fade Q_{loss} against the full eq. cycles FEC, Fig. 11, it is clear that the relative degradation per cycle ($\frac{\partial Q_{loss}}{\partial FEC}$) of the *CPBDeg* is the smallest of them all. Moreover, its empirical competitor (*CEmpDeg*) has the highest degradation per cycle $\frac{\partial Q_{loss}}{\partial FEC}$, having the most inefficient degradation control. This appears to be a risky strategy due to a lack of consistency across seasons and objectives (minimizing degradation or minimizing grid costs). Lastly, even though the capacity fade is not significant in $T = 1$ month, daily optimization can have a significant impact in the long term, as it was shown in [39,49,50]. As a final note, if the C-rate is increased (≥1) and battery temperature $T_{b,t}$ is not constant, the degradation on a daily basis can be significantly higher.

Finally, the computational time for the different strategies is presented in Fig. 12. Each sample is the total computational time it takes to solve Algorithm 2. All OCP instances are solved until local optimality, with *BNoDeg* being the closest to its global optima since its a convex QCQP [67]. Unexpectedly, *BNoDeg* has the lowest and most consistent t_{comp} distribution, i.e., the smallest standard deviation. Both *CEmpDeg* and *CPBDeg* planners have similar distributions, maintaining overall fast computational time between 1–5 s. More importantly, all three distributions overlap with more than 50% of cumulative probability. The optimization model variables and equations after transcription are presented in terms of their number of variables in Table 4. Hence, the increase in modelling accuracy of PBROM is not prohibitively expensive when compared to its empirical counterpart. This is to be expected as the empirical ageing model is also non-linear and non-convex. All of these demonstrates the feasibility of implementing the *CPBDeg* in real-time applications.

Table 4
Problem size and variables after discretization for each planner.

	BNoDeg	CEmpDeg	CPBDeg
# Variables	4416	6720	6720
# Constraints	3073	5377	5377
# Linear Eq.	2113	4033	4033
# Quad. Eq.	768	768	768
# Nonlin. Eq.	0	384	384
# Linear Ineq.	192	192	192

In summary, this case study shows that:

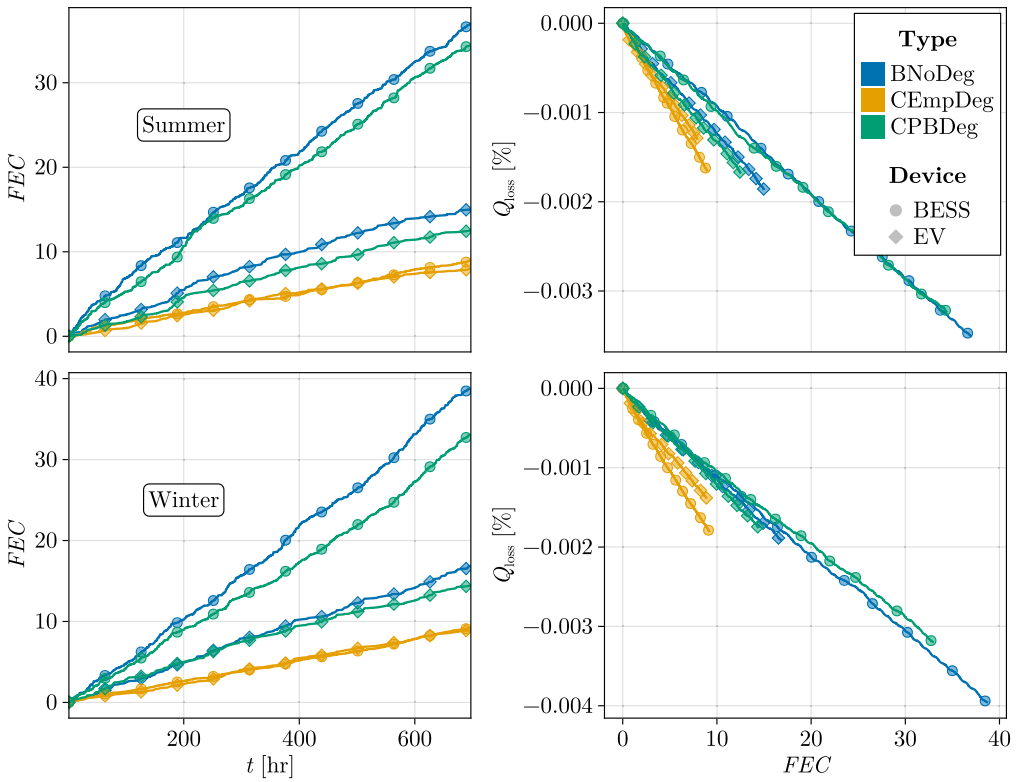

Fig. 11. Full equivalent cycles FEC over time (left) and relative capacity fade Q_{loss} over FEC (right).

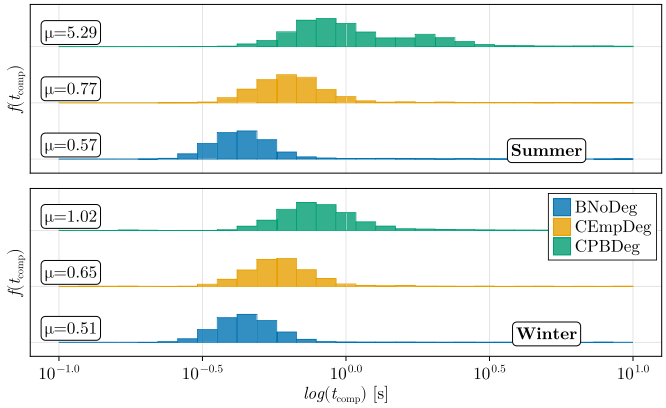

Fig. 12. Distributions of computational time t_{comp}.

- *CPBDeg* achieves the smallest $\frac{\partial Q_{\text{loss}}}{\partial FEC}$ (best ageing control) while maintaining close to best C_{grid}.
- The computational cost of *CPBDeg* is not prohibitive when compared to its benchmarks.
- *BNoDeg* achieves the smallest C_{grid} with fast computational times, as expected.

5.2. Case study II: Managing different cathodes

To demonstrate the PB models' flexibility and extended capabilities, the *CPBDeg* controller is tested using two similar battery packs of the same rated capacity Q but using different cells. One is formed with NMC cells and the other with LFP. Since LFP cells have a lower rated capacity of $Q_n = 2.3$ Ah and a lower OCV, the battery packs have more $N_{s/p}$ to have roughly the same pack-rated capacity as their NMC counterparts. The power limits $\overline{P}_{b,t}$, $\underline{P}_{b,t}$ are also maintained to make an even comparison. Another weight w_{loss} is chosen to further highlight differences between cathode chemistries. The driving profile (availability and consumption) are different from the previous Section, thus small deviations in costs are expected.

The PB ageing models are suitable for both because they have graphite anodes [15,33]. Nevertheless, they have different electrolytes. This is addressed by changing the electrolyte parameters in the model. The same model equations are used, but with different parameter values. This is a great advantage compared to the empirical fits presented in the literature. In the latter, the derived models are prone to overfitting to training conditions, delivering complex non-linear equations that can only be applied to specific chemistries and operating conditions (stationary loads, fixed states).

The simulation results are presented in Figs. 13–15. Starting with the EV, Fig. 13, the operation is similar except for a few days in summer and winter in which the LFP decides to have deeper discharges than its NMC counterpart. In other words, the actions in the NMC case are more conservative since the NMC is more sensitive to the SEI degradation.

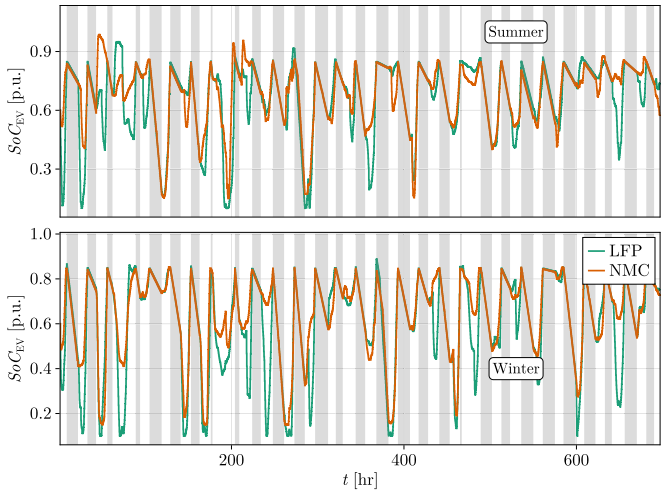

Fig. 13. Cathode comparison simulation SoC_{EV}. Grey bands indicate driving periods.

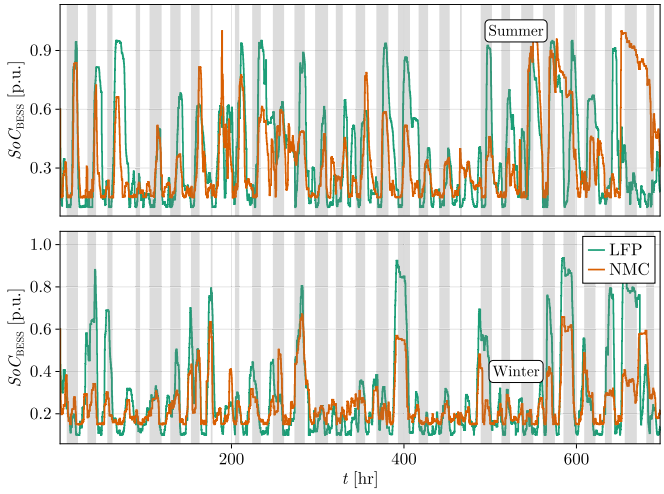

Fig. 14. Cathode comparison simulation SoC_{BESS}.

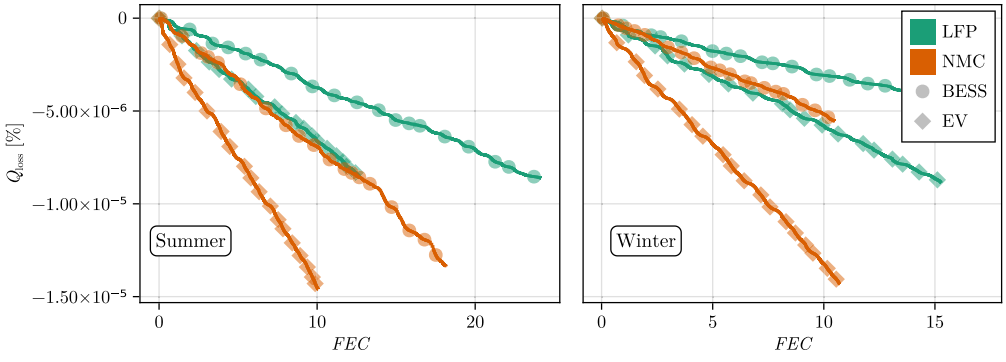

Fig. 15. Case Study 2 - LFP and NMC cells degradation analysis.

Moreover, with the LFP cells the *CPBDeg* chooses to do V2G more often than with the NMC cell. These leads to the *CPBDeg-LFP* achieving lower grid costs C_{grid} due to the increased throughput.

Continuing with the ageing analysis Fig. 15 presents the FEC and Q_{loss} results. The overall the FEC are increased with the LFP cells. In combination with its lower calendar ageing, represented in the parameter set, the LFP packs achieve lower degradation per eq. cycle $\frac{\partial Q_{loss}}{\partial FEC}$ than their NMC counterpart. As such, the *CPBDeg-LFP* increases both BESS and EV total throughput (FEC) while reducing its degradation Q_{loss}. Overall the change in cathode and consequent electrolyte, reduces the SEI degradation rate resulting in a more effective degradation control.

Table 5 presents the summary of performance for both cell types. Overall, the *CPBDeg-LFP* achieves lower total grid costs and ageing. During winter C_{grid} stays the same (≈4%) while the LFP cells has 20% less degradation. However, in the summer, the LFP C_{grid} is 10% smaller than its NMC counterpart, with C_{grid} similar to *BNoDeg* in Section 5.1 Table 3. The LFP summer case also has also roughly 20% less capacity

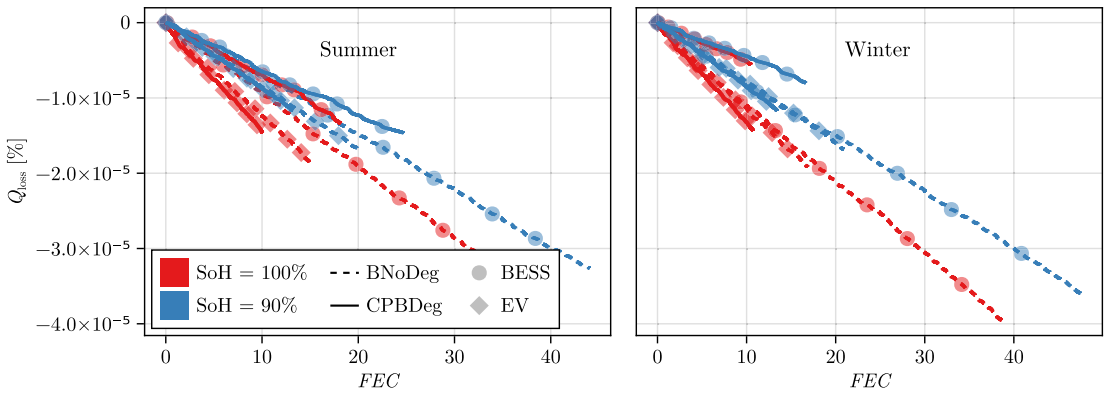

Fig. 16. Case Study 3 - new and aged cells degradation analysis.

Table 5
Cathode comparison cost summary with weights $w_{grid} = 1$, $w_{SoC} = w_{TESS} = 1000$.

$w_{loss} = 0.1$	C_g [€]		Q_{loss} [mAh]	
Cell cathode	summer	winter	summer	winter
LFP	57.9	112.0	186.7	170.5
NMC	64.7	116.9	243.0	210.2

Table 6
Cost and degradation summary with weights $w_{grid} = 1$, $w_{loss} = 0.1$, $w_{SoC} = w_{TESS} = 1000$.

Planner	C_g [€]		Q_{loss} [mAh]	
	summer	winter	summer	winter
SoH 100%				
BNoDeg	55.39	101.66	377.31	400.14
CPBDeg	64.68	116.86	242.92	210.18
SoH 90%				
BNoDeg	58.66	111.31	281.11	288.31
CPBDeg	60.87	120.86	168.64	149.30

fade than its NMC benchmark. This shows that *CPBDeg* rightly exploits its physical information of the system to achieve better performance, both lower grid cost and lower capacity fade.

5.3. Case study III: Managing aged and fresh batteries

To demonstrate the flexibility and extended capabilities of the *CPBDeg* planner the scheduler is tested using two battery packs: the first is the fresh battery pack of NMC cells of Section 5.1 and the second is the same pack but with cells aged at $SoH = 90\%$. Only one benchmark is used: a *BNoDeg* with no SoH update. Thus, the *BNoDeg* EMS sees a perfectly healthy cell with rated capacity when in reality the battery pack is aged 10%. There is no empirical benchmark because the only parameter that can be update in it is the initial lifetime $t_{0,b}$, only affecting calendar ageing. The update is based on a 5% increase in series resistance $R_{b,0}$ and 10% decrease of the available Li content $z_{100\%,b}$ and its propagation with the equations of Section 3.3.2.

Fig. 16 presents the degradation patterns for the 2 planners and different SoH. In the aged battery, the share of calendar ageing (against the total) within $i_{SEI,b,t}$ is much smaller and thus the percentual Q_{loss} is almost 25% smaller than in the new battery packs. In both seasons, the EVs patterns are similar for both *BNoDeg* and *CPBDeg*. The change in EV trajectories between aged and fresh cells shows a slight increase FEC, due to a smaller rated capacity, and a decrease in relative ageing, due to reduced calendar ageing. The impact on the BESS is more pronounced. In winter, *CPBDeg* has a smaller $\frac{\partial Q_{loss}}{\partial FEC}$ (upper-right hand side of the graph) for both aged and new cells, with *BNoDeg* doing more eq. cycles. In the winter *CPBDeg* still has a smaller $\frac{\partial Q_{loss}}{\partial FEC}$ in the new cell but not in the used cell, where this is achieved by the benchmark controller. In other words, as the battery ages, the predominance of calendar ageing within the SEI layer is diminished. Thus, the link between $i_{b,t}$ and $Q_{loss,b,t}$ becomes stronger, due to the predominance of active material loss and the cyclic component of the SEI layer.

For the current simulation time T of 1 month and average C-rate below 1C, the degradation slope may appear linear to the naked eye. However, in Fig. 16, the trajectory of the aged battery is also presented, and its average slope is smaller than the new battery degradation slope ($\frac{\Delta Q_{loss,b}}{\Delta FEC_b}|_{SoH=90\%} < \frac{\Delta Q_{loss,b}}{\Delta FEC_b}|_{SoH=100\%}$). This is due to the nonlinear dependency of $i_{SEI,b,t}$ with $\sqrt{t}$. Thus, it is clear that even though each trajectory might appear linear, over longer simulation times of several months and years, the dependency is non-linear.

Finally, when adding the costs to the analysis, summarized in Table 6, the *CPBDeg* achieves lower capacity fade Q_{loss} than *BNoDeg* across all seasons and SoH (between 30%–45% less). Even improving the total grid cost C_{grid} by 6% in the summer as the cells degrades. On the other hand, *BNoDeg* worsens its performance as the cells degrade with higher C_{grid} (6%–9%), Q_{loss} and model bias.

In summary, the performance of the proposed *CPBDeg* eMPC controller comparatively improves when using used cells, with respect to its linear *BNoDeg* benchmark. This is because the ageing PBROMs encapsulate the fade of calendar ageing ($\sqrt{t}$) and rise of cyclic SEI and AM ($i_{b,t}, SoC_{b,t}$) as the battery ages.

5.4. Limitations & Future works

As it was mentioned in Section 3 two major assumptions are made regarding the battery packs: (i) moderate C-rates of less than 1C, (ii) constant comfortable battery pack temperature. Both allow us to neglect important factors, such as Li-plating. Temperature control is part of the local primary controls performed by the respective BMS and no-fast charging outside of the house assumed. Of course, they limit the extension of the presented results to specific days of high heat or low temperatures, since other degradation mechanisms will play a more relevant role. Moreover, as the operation bounds grow more extreme (C-rate and temperatures), the less accurate the models grow even PB models. Future research could explore active thermal controls and their impact on the presented degradation control.

The thermal flow-based models used in this paper assume a fixed building temperature decided externally, that produces the exogenous thermal load P^{th}_{load}. Another thermal limitation is that efficiencies and conversion factors are assumed linear. These limits the presented work thermal flexibility, since the building's thermal capacity could be used as a passive thermal storage and HP consumption prediction could be improved. Both are explored in other works such as [30,47].

A natural limitation of all model-based optimal control methods is that they rely on accurate uncertainty estimation techniques. This means that accurate forecasters are needed to feed belief states $\tilde{B}_t$ of inputs W_{t+1} and state observers/estimators to feedback state measurements $S_{a,t+1}$ and accurately parametrize the transition functions $\tilde{S}_t^M(\cdot)$. The accuracy of both the forecasts $\tilde{B}_t$ and device models $\tilde{S}_{a,t}^M(\cdot)$ is a necessary condition for successful real-life policies. The development of battery observers is outside of the scope of this paper but the reader might refer to [40,56,57,70]. The experimental validation of particular models used is outside of the scope of this paper, since we do not want to contribute with a new battery model but with a new dispatch algorithm. The core idea of the present paper is showing that ageing PBROMs, such as the one developed by Jin [15] or similar, can be integrated to wider EMS/control schemes.

Regarding the periodic constraints of the BESS and TESS. Even though the terminal set of the BESS is more flexible than the standard literature, the design is still arbitrary. It would be interesting to design the terminal conditions as part of a wider control scheme, such as seasonal optimization [69]. Not only for the BESS but for the TESS, since due to the $H^{\text{DA}} = 48\text{hs}$, $H^{\text{MPC}} = 24\text{hs}$ its low short-term efficiency leads to discharging and not cycling the TESS.

The practical implications for residential consumers are twofold: the short-term grid-cost savings often come at the expense of accelerated battery aging. While the *BNoDeg* and *CEmpDeg* controller can yield lower monthly grid costs (C_{grid}), they do so by aggressively cycling the battery in ways that ignore internal degradation mechanisms. By utilizing the *CPBDeg* control, users can transition from a short-sighted "bill minimization" strategy to a "Total Cost of Ownership" (TCO) approach. Given the capacity fade cost of approximately 300 €/kWh, the ability of the PBROM-based EMS to reduce degradation per cycle ($\partial Q_{\text{loss}}/\partial FEC$) suggests that the battery's operational lifespan could be extended by several years. This significantly improves the Net Present Value (NPV) of the residential energy system and reduces the frequency of capital-intensive storage replacements. Naturally, further work is needed to implement similar schemes in real life and until then this work acts as a benchmark to highlight potential savings or practical recommendations. These include, choosing LFP battery packs or maintaining batteries close to their $\underline{SoC}_{b,t}$.

6. Conclusions & Discussion

In summary, this paper presents an optimization-based non-linear eMPC for residential multi-carrier energy systems that uses PBROM models to integrate battery ageing. Its integration with the thermal and mobility carriers is achieved by designing specific terminal sets for the individual storage systems, depending on their use and technology. The proposed *CPBDeg* control can handle different cathode chemistries as well as batteries in different ageing states. The controller can do this with lower degradation than the benchmarks, by increasing w_{loss}. The PBROM integration comes at the expense of slightly higher computational times and grid cost in the case of NMC cells.

In the first case study, it is shown how advanced PBROM can be used to reduce battery ageing while maintaining a grid cost comparable to benchmarks, in accordance with the literature for standalone utility-scale applications [28,38,39,42,71]. Moreover, the *CPBDeg* has the most smallest capacity fade per cycle. This is because the control can effectively relate actions to degradation states.

In the second case study, the proposed planner is equipped with battery packs of different cathode chemistries, and its performance is compared. Empirical models are cathode-specific and thus cannot handle multiple cell chemistries. The LFP battery pack has a lower total Q_{loss} as per established knowledge and can achieve lower grid costs C_{grid} than its NMC counterpart. Even more so, when considering that the relative cost c_{loss} for both packs was the same, when in reality LFP packs have a lower cost than NMC packs. Thus, Section 5.2 is a conservative approximation, and LFP packs have the potential to enable even lower TCO. The grid savings are achieved just by changing some simple model parameters taken from the literature. This flexibility is an essential feature because it allows the EMS to exploit any battery pack at hand fully. This directly impacts the choice of the residential users towards LFP battery packs, because even without aging-aware controls the overall ageing favours LFP packs which is already an industry standard.

The last case study showed how the proposed EMA handles aged and new batteries seamlessly, even improving performance as the battery ages, improving the summer grid cost by 6%. The reason is that the EMA can identify predominant degradation mechanisms from the ageing PBROM, exploiting the decrease of SEI importance over time and the rise of active material loss. Its linear counterpart, however, is unaware of the degradation causing the energy costs to increase. Summing up, grid costs can be reduced by using LFP battery packs or modifying objective weights, the latter at the expense of higher degradation. Finally, the integration of ageing PBROMs has a low impact on the HP and TESS, meaning that the grid cost savings during summer of Section 5.2 are achieved without fundamentally modifying the thermal strategy. In applications where scalability and fast computation are key drivers, decomposition strategies could be explored to exploit this coupling.

On a broader scope, even though relevant challenges are still pending or out of the scope of this paper, this paper aims to show the potential savings enabled by aging-aware control laws in the residential sector. The findings presented here can be easily transferred to other sectors such as commercial or industry, which might have more tools to implement complex EMS.

For physical setups the proposed physics-based approach requires a non-linear observer to identify internal states and a system identification algorithm to parametrize the models. Adaptive control techniques/online learning techniques are crucial for scaling implementation. For the case of the BESS initial tests and model identification can be done offline before start-up, and even offline during operation if historic data is continuously stored. However, for EVs models, parametrization deems a challenge since a previously unknown car may appear or due to unknown driving conditions and profiles. Thus, the development of effective and accurate observers to identify and parametrize PBROM online automatically is crucial.

CRediT authorship contribution statement

Darío Slaifstein: Writing – review & editing, Writing – original draft, Visualization, Validation, Software, Methodology, Investigation, Formal analysis, Data curation, Conceptualization. **Gautham Ram Chandra Mouli:** Writing – review & editing, Supervision, Project administration, Funding acquisition. **Laura Ramirez-Elizondo:** Writing – review & editing, Supervision, Funding acquisition. **Pavol Bauer:** Supervision, Project administration, Funding acquisition.

Declaration of Generative AI and AI-assisted technologies in the writing process

During the preparation of this work, the author(s) used ChatGPT and Gemini to help the writing process in favour of clarity and readability. After using this tool/service, the author(s) reviewed and edited the content as needed and take(s) full responsibility for the content of the published article.

Declaration of competing interest

The authors declare the following financial interests/personal relationships which may be considered as potential competing interests: Dario Slaifstein reports financial support was provided by Ministry of Economic Affairs and Climate Policy. If there are other authors, they declare that they have no known competing financial interests or personal relationships that could have appeared to influence the work reported in this paper.

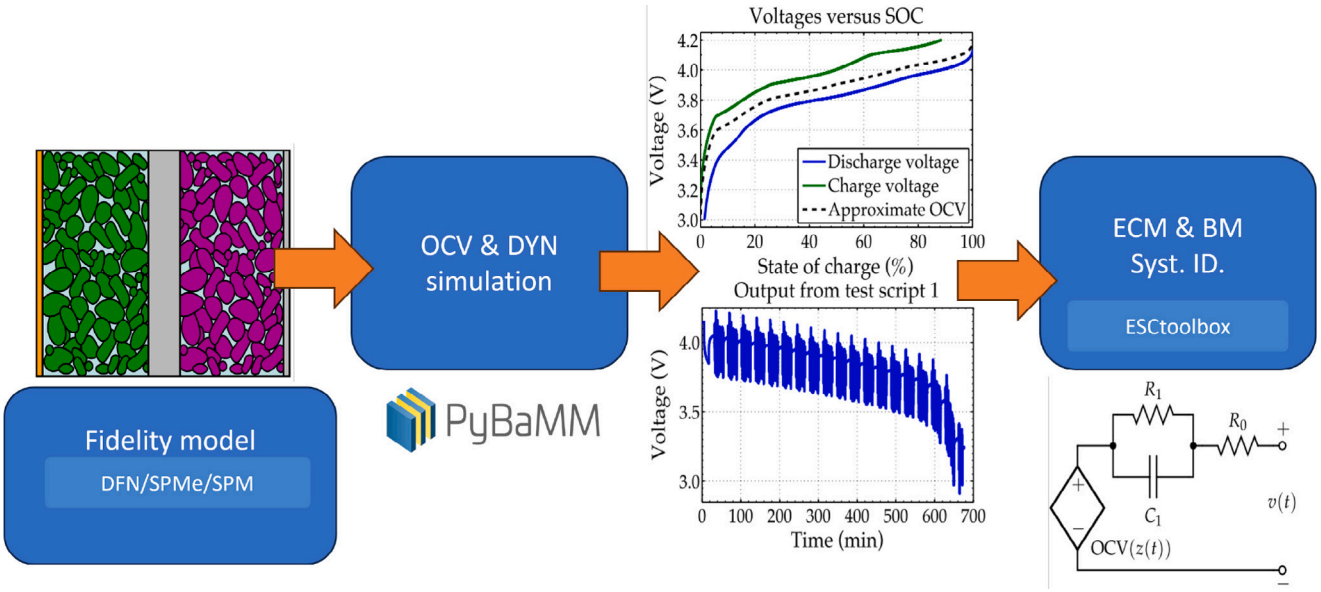

Fig. A.17. ECM System Identification pipeline used to build planner models.

Acknowledgement

The project was carried out with a Top Sector Energy subsidy from the Ministry of Economic Affairs and Climate, carried out by the Netherlands Enterprise Agency (RVO). The specific subsidy for this project concerns the MOOI subsidy round 2020, FLEXINet project grant number MOOI 32027.

Appendix A. Building battery models

Graphite anode open-circuit voltage [15,33]:

$$\begin{aligned} OCV_{n,b,t}(z_{b,t}) = {} & 0.6379 + 0.5416 \cdot e^{-305.5309 \cdot z_{b,t}} \\ & + 0.044 \cdot \tanh\left(-\frac{z_{b,t} - 0.1958}{0.108}\right) \\ & - 0.1978 \cdot \tanh\left(\frac{z_{b,t} - 1.0571}{0.0854}\right) \\ & - 0.6875 \cdot \tanh\left(\frac{z_{b,t} + 0.0117}{0.0529}\right) \\ & - 0.0175 \cdot \tanh\left(\frac{z_{b,t} - 0.5692}{0.0875}\right) \end{aligned} \tag{38}$$

Table A.7 presents the model parameters for the PBROMs.

For the first-order ECMs the model parameters are presented in Table A.8.

In order to test the each of the EMS decision-making a virtual simulator is necessary to stablish a common ground to compare policies [45]. A reasonable tool is the `PyBaMM` modelling and simulation library as a digital simulator, which is widely used in the battery community for design, optimization and benchmarking [62]. `PyBaMM` has datasets for several real cells, including NMC and LFP cells [32,34].

To construct the models used in the optimizer, $\tilde{S}^{M}_{b,t}(\cdot)$, and avoid using physical cells, one can use a PyBaMM model (compendium of PDEs) and simulate dynamic and open circuit tests as the ones specified in [18], and identify an ECM using system identification with the `ESCtoolbox`, again following [18]. The pipeline is presented in Fig. A.17.

To build the simulator, $S^{M}_{b,t}(\cdot)$, directly using PyBaMM is inconvenient because interfacing `Julia` and `Python` is possible but hinders execution time. The solution is using the `LiiBRA.jl` package [54], which builds a state-space PBROM from the SPM or DFN model using Discrete-time Realization Algorithms (DRA). This greatly improves simulation times and allows for detailed simulations with a time resolution of $\Delta t_s = 1$s [54].

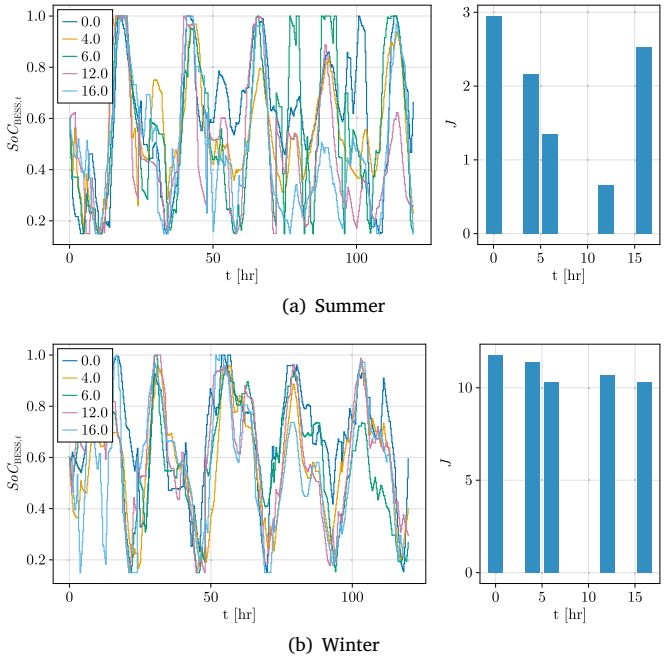

(a) Summer

(b) Winter

Fig. B.18. BESS State-of-Charge $SoC_{\text{BESS},t}$ and total objective J as a function of terminal condition t_1 in (a) summer and (b) winter.

Appendix B. Periodic condition

In Eq. (18) the value of $t_1 = 6$hs was chosen experimentally through simulations. Fig. B.18 presents the $SoC_{\text{BESS},t}$ and the total objective J as function of terminal condition t_1 for the standard (mean inputs) weeks of summer and winter. In it, the $t_1 = 6$hs maintains the second place in both weeks, with its closest competitor of $t_1 = 12$hs is dependent of solar generation which plummets in winter.

Table A.7
Parameter values, descriptions, and units for PBROMs.

Parameter	Description	Units	NMC (SANYO cell)	LFP (A123 cell)
n_{SEI}	Number of e^- transferred in SEI side reaction	–	2.0	
λ	Constant $\lambda = \frac{c_s\sqrt{D_s}}{c_p\sqrt{D_p}}$	–	5.51×10^{-5}	
OCV_s	OCV of the side reaction	V	0.4	
ϵ_{AM}	Active material volume fraction	–	0.552	
R_s	Particle radius	m	7.5×10^{-6}	5×10^{-6}
a_s	Specific surface area of the anode	m^{-1}	$\frac{3\cdot\epsilon_{AM}}{R_s}$	
A_n	Active surface area of the anode	m^2	0.105	0.18
L_n	Thickness of anode	m	50×10^{-6}	34×10^{-6}
i_0	Exchange current of the intercalation current	A/m^2	1.5	
k_{SEI}	Kinetic rate	$1/\sqrt{s}$	66.85	
E_{SEI}	Activation energy	J/mol	39146.0	
$\delta_{SEI,0}$	Initial value of the SEI layer thickness	m	2.0×10^{-9}	
M_{SEI}	Molecular weight of the SEI layer	kg/mol	0.162	
ρ_{SEI}	Density of the SEI layer	kg/m^3	1690.0	
$z_{100\%}$	Full electrode stoichiometry	–	0.9	0.81
$z_{0\%}$	Empty electrode stoichiometry	–	0	0.0176
k_{AM}	Kinetic rate	1/Ah	0.0137	
E_{AM}	Activation energy	J/mol	39500.0	
β	Tuning parameter	–	1.7	
t_0^+	Transport/transference number	–	0.363	0.36
E_κ	Activation energy for κ	J/mol	34700.0	
E_{D_e}	Activation energy for D_e	J/mol	34700.0	
κ_{ref}	Reference ionic conductivity for κ at reference temperature	S/m	0.174	
$D_{e,ref}$	Reference value for D_e at reference temperature	m^2/s	7.5×10^{-11}	
$brug$	Bruggeman coefficient	–	3/2	
$c_{e,avg}$	Average volume concentration of Li in the electrolyte	mol/m^3	1000	1200
$c_{e,max}$	Maximum volume concentration of Li in the electrolyte	mol/m^3	1000	1200
σ_n	Electronic conductivity	S/m	100	215
ϵ_s	Volume fraction of solid electrolyte	–	0.59	0.58

Table A.8
Parameter values, descriptions, and units for ECMs.

Parameter	Unit	NMC (SANYO cell)	LFP (A123 cell)
η_c	%	99.5	99.9
Q_0	Ah/cell	5.29	2.29
R_0	mΩ	28.11	27.01
$\tau_1 = R_1C_1$	s	2.35	2.13
R_1	mΩ	33.57	26.98

Data availability

The url and name are https://github.com/DarioSlaifsteinSk/AgeRMCES and AgeRMCES respectively.

References

[1] IEA, Net Zero by 2050: A Roadmap for the Global Energy Sector, International Energy Agency, 2021, p. 224.

[2] M. Geidl, G. Andersson, Optimal power flow of multiple energy carriers, IEEE Trans. Power Syst. 22 (1) (2007) 145–155, http://dx.doi.org/10.1109/TPWRS.2006.888988, URL https://ieeexplore.ieee.org/document/4077107/.

[3] G. Andersson, E. Zurich, M. Geidl, Optimal power dispatch and conversion in systems with multiple energy carriers PlanGridEV view project BPES-optimal sizing and control of balancing power in the future EU power system considering transmission constraints view project OPTIMAL POWER DISPATC, in: Proceedings 15th Power Systems Computation Conference (PSCC), 2005, URL https://www.researchgate.net/publication/228776936.

[4] W. Vermeer, G.R.C. Mouli, P. Bauer, Real-time building smart charging system based on PV forecast and li-ion battery degradation, Energies 13 (13) (2020) 3415, http://dx.doi.org/10.3390/EN13133415, 13 (13) (2020) 3415 URL https://www.mdpi.com/1996-1073/13/13/3415/htm, https://www.mdpi.com/1996-1073/13/13/3415.

[5] W. Vermeer, G.R. Chandra Mouli, P. Bauer, A comprehensive review on the characteristics and modeling of lithium-ion battery aging, IEEE Trans. Transp. Electrification 8 (2) (2022) 2205–2232, http://dx.doi.org/10.1109/TTE.2021.3138357, URL https://ieeexplore.ieee.org/document/9662298/.

[6] G. Ceusters, R.C. Rodríguez, A.B. García, R. Franke, G. Deconinck, L. Helsen, A. Nowé, M. Messagie, L.R. Camargo, Model-predictive control and reinforcement learning in multi-energy system case studies, Appl. Energy 303 (2021) 117634, http://dx.doi.org/10.1016/j.apenergy.2021.117634, URL https://linkinghub.elsevier.com/retrieve/pii/S0306261921010011.

[7] G. Ceusters, L.R. Camargo, R. Franke, A. Nowé, M. Messagie, Safe reinforcement learning for multi-energy management systems with known constraint functions, Energy AI 12 (2023) 100227, http://dx.doi.org/10.1016/j.egyai.2022.100227, URL https://linkinghub.elsevier.com/retrieve/pii/S2666546822000738.

[8] D. Van Der Meer, G.R.C. Mouli, G.M.E. Mouli, L.R. Elizondo, P. Bauer, Energy management system with PV power forecast to optimally charge EVs at the workplace, IEEE Trans. Ind. Inform. 14 (1) (2018) 311–320, http://dx.doi.org/10.1109/TII.2016.2634624.

[9] Y. Ye, D. Qiu, X. Wu, G. Strbac, J. Ward, Model-free real-time autonomous control for a residential multi-energy system using deep reinforcement learning, IEEE Trans. Smart Grid 11 (4) (2020) 3068–3082, http://dx.doi.org/10.1109/TSG.2020.2976771, URL https://ieeexplore.ieee.org/document/9016168/.

[10] W. Vermeer, G.R.C. Mouli, P. Bauer, Optimal sizing and control of a PV-EV-BES charging system including primary frequency control and component degradation, IEEE Open J. Ind. Electron. Soc. 3 (2022) 236–251, http://dx.doi.org/10.1109/OJIES.2022.3161091, URL https://ieeexplore.ieee.org/document/9740621/.

[11] W. Vermeer, G.R. Chandra Mouli, P. Bauer, A multi-objective design approach for PV-battery assisted fast charging stations based on real data, IEEE Transp. Electrification Conf. Expo, ITEC 2022 (2022) 114–118, http://dx.doi.org/10.1109/ITEC53557.2022.9814016.

[12] A. Esmaeel Nezhad, A. Rahimnejad, P.H.J. Nardelli, S.A. Gadsden, S. Sahoo, F. Ghanavati, A shrinking horizon model predictive controller for daily scheduling of home energy management systems, IEEE Access 10 (2022) 29716–29730, http://dx.doi.org/10.1109/ACCESS.2022.3158346, URL https://ieeexplore.ieee.org/document/9732346/.

[13] P. Alexeenko, E. Bitar, Achieving reliable coordination of residential plug-in electric vehicle charging: A pilot study, Transp. Res. Part D: Transp. Environ. 118 (2023) 103658, http://dx.doi.org/10.1016/j.trd.2023.103658, URL https://linkinghub.elsevier.com/retrieve/pii/S136192092300055X.

[14] M.A. Xavier, A.K. de Souza, K. Karami, G.L. Plett, M.S. Trimboli, A computational framework for lithium ion cell-level model predictive control using a physics-based reduced-order model, IEEE Control. Syst. Lett. 5 (4) (2021) 1387–1392, http://dx.doi.org/10.1109/LCSYS.2020.3038131, URL https://www.ieee.org/publications/rights/index.html, https://ieeexplore.ieee.org/document/9259035/.

[15] X. Jin, Aging-aware optimal charging strategy for lithium-ion batteries: Considering aging status and electro-thermal-aging dynamics, Electrochim. Acta 407 (2022) 139651, http://dx.doi.org/10.1016/j.electacta.2021.139651, URL https://linkinghub.elsevier.com/retrieve/pii/S0013468621019356.

[16] Y. Li, Y. Yang, J. Tang, B. Xiong, X. Deng, D. Tang, Design of degradation-conscious optimal dispatch strategy for home energy management system with rooftop PV and lithium-ion batteries, in: 2019 4th International Conference

on Intelligent Green Building and Smart Grid, IGBSG, IEEE, 2019, pp. 741–746, http://dx.doi.org/10.1109/IGBSG.2019.8886194, URL https://ieeexplore.ieee.org/document/8886194/.

[17] G.L. Plett, Battery management systems volume I battery modeling, in: Artech House Power Engineering and Power Electronics, 2015, URL https://us.artechhouse.com/Battery-Management-Systems-Volume-1-Battery-Modeling-P1752.aspx.

[18] G.L. Plett, BATTERY management SYSTEMS volume II: Equivalent-circuit methods, in: Artech House Power Engineering and Power Electronics, first ed., 2016, URL https://us.artechhouse.com/Battery-Management-Systems-Volume-II-Equivalent-Circuit-Methods-P2192.aspx.

[19] Z. Chen, L. Wu, Y. Fu, Z. Chen, L. Wu, Real-time price-based demand response management for residential appliances via stochastic optimization and robust optimization, IEEE Trans. Smart Grid 3 (2012) http://dx.doi.org/10.1109/TSG.2012.2212729.

[20] M.J. Risbeck, Mixed-integer model predictive control with applications to building energy systems, (Ph. D. thesis), 2018, URL https://digital.library.wisc.edu/1711.dl/HYZKXNHJKGARE8C.

[21] T. Jouini, A. Bensmann, T. Lilge, R. Hanke-Rauschenbach, M. Müller, Predictive operation of multi-energy systems in sequential markets: A case study, in: 2024 European Control Conference, ECC, IEEE, 2024, pp. 1509–1515, http://dx.doi.org/10.23919/ECC64448.2024.10591115, URL https://ieeexplore.ieee.org/document/10591115/.

[22] P. Li, T. Guo, M. Abeysekera, J. Wu, Z. Han, Z. Wang, Y. Yin, F. Zhou, Intraday multi-objective hierarchical coordinated operation of a multi-energy system, Energy 228 (2021) 120528, http://dx.doi.org/10.1016/j.energy.2021.120528, URL https://linkinghub.elsevier.com/retrieve/pii/S0360544221007775.

[23] D. Mariano-Hernández, L. Hernández-Callejo, A. Zorita-Lamadrid, O. Duque-Pérez, F. Santos García, A review of strategies for building energy management system: Model predictive control, demand side management, optimization, and fault detect & diagnosis, J. Build. Eng. 33 (2021) 101692, http://dx.doi.org/10.1016/j.jobe.2020.101692, URL https://linkinghub.elsevier.com/retrieve/pii/S2352710220310627.

[24] S. Yang, H.O. Gao, F. You, Building electrification and carbon emissions: Integrated energy management considering the dynamics of the electricity mix and pricing, Adv. Appl. Energy 10 (2023) 100141, http://dx.doi.org/10.1016/J.ADAPEN.2023.100141, URL https://www-sciencedirect-com.tudelft.idm.oclc.org/science/article/pii/S2666792423000203#fig0001.

[25] M. Mittelviefhaus, G. Georges, K. Boulouchos, Electrification of multi-energy hubs under limited electricity supply: De-/centralized investment and operation for cost-effective greenhouse gas mitigation, Adv. Appl. Energy 5 (2022) 100083, http://dx.doi.org/10.1016/J.ADAPEN.2022.100083, URL https://www.sciencedirect.com/science/article/pii/S2666792422000014.

[26] Q. Su, Z. Gao, Z. Zhong, Dynamic energy hub-based planning and operation for optimal integration of variable energy conversion efficiency in community-level energy systems, Energy 332 (2025) 137143, http://dx.doi.org/10.1016/j.energy.2025.137143, URL https://linkinghub.elsevier.com/retrieve/pii/S0360544225027859.

[27] A. Karthikeyan, V. Arun, Enhancing energy hub management with unified plug-in electric vehicle based demand response and energy storage systems, J. Energy Storage 108 (2025) 114997, http://dx.doi.org/10.1016/j.est.2024.114997, URL https://www-sciencedirect-com.tudelft.idm.oclc.org/science/article/pii/S2352152X24045833?via%3Dihub#f0015.

[28] J.M. Reniers, G. Mulder, D.A. Howey, Review and performance comparison of mechanical-chemical degradation models for lithium-ion batteries, J. Electrochem. Soc. 166 (14) (2019) A3189–A3200, http://dx.doi.org/10.1149/2.0281914jes, URL https://iopscience.iop.org/article/10.1149/2.0281914jes.

[29] V. Vega-Garita, M. Heydarzadeh, A.H. Dadash, E. Immonen, The need for aging-aware control methods in lithium-ion batteries: A review, J. Energy Storage 132 (2025) 117653, http://dx.doi.org/10.1016/J.EST.2025.117653, URL https://www.sciencedirect.com/science/article/pii/S2352152X25023667?via%3Dihub.

[30] J. Alpízar-Castillo, L.M. Ramírez-Elizondo, P. Bauer, Modelling and evaluating different multi-carrier energy system configurations for a dutch house, Appl. Energy 364 (2024) 123197, http://dx.doi.org/10.1016/j.apenergy.2024.123197, URL https://linkinghub.elsevier.com/retrieve/pii/S0306261924005804.

[31] Y. Li, D.M. Vilathgamuwa, D.E. Quevedo, C.F. Lee, C. Zou, Ensemble nonlinear model predictive control for residential solar battery energy management, IEEE Trans. Control Syst. Technol. 31 (5) (2023) 2188–2200, http://dx.doi.org/10.1109/TCST.2023.3291540, URL https://ieeexplore.ieee.org/document/10186024/.

[32] S.E.J. O'Kane, W. Ai, G. Madabattula, D. Alonso-Alvarez, R. Timms, V. Sulzer, J.S. Edge, B. Wu, G.J. Offer, M. Marinescu, Lithium-ion battery degradation: how to model it, Phys. Chem. Chem. Phys. 24 (13) (2022) 7909–7922, http://dx.doi.org/10.1039/D2CP00417H, URL http://xlink.rsc.org/?DOI=D2CP00417H.

[33] X. Jin, A. Vora, V. Hoshing, T. Saha, G. Shaver, R.E. García, O. Wasynczuk, S. Varigonda, Physically-based reduced-order capacity loss model for graphite anodes in li-ion battery cells, J. Power Sources 342 (2017) 750–761, http://dx.doi.org/10.1016/j.jpowsour.2016.12.099, URL https://linkinghub.elsevier.com/retrieve/pii/S037877531631802X.

[34] E. Prada, D. Di Domenico, Y. Creff, J. Bernard, V. Sauvant-Moynot, F. Huet, A simplified electrochemical and thermal aging model of LiFePO 4 - graphite li-ion batteries: Power and capacity fade simulations, J. Electrochem. Soc. 160 (4) (2013) A616–A628, http://dx.doi.org/10.1149/2.053304JES/XML, URL https://iopscience.iop.org/article/10.1149/2.053304jes, https://iopscience.iop.org/article/10.1149/2.053304jes/meta.

[35] J. Wang, J. Purewal, P. Liu, J. Hicks-Garner, S. Soukazian, E. Sherman, A. Sorenson, L. Vu, H. Tataria, M.W. Verbrugge, Degradation of lithium ion batteries employing graphite negatives and nickel–cobalt–manganese oxide + spinel manganese oxide positives: Part 1, aging mechanisms and life estimation, J. Power Sources 269 (2014) 937–948, http://dx.doi.org/10.1016/j.jpowsour.2014.07.030, URL https://linkinghub.elsevier.com/retrieve/pii/S037877531401074X.

[36] J. Schmalstieg, S. Käbitz, M. Ecker, D.U. Sauer, A holistic aging model for li(NiMnCo)o2 based 18650 lithium-ion batteries, J. Power Sources 257 (2014) 325–334, http://dx.doi.org/10.1016/j.jpowsour.2014.02.012, URL https://linkinghub.elsevier.com/retrieve/pii/S0378775314001876.

[37] J. Purewal, J. Wang, J. Graetz, S. Soukiazian, H. Tataria, M.W. Verbrugge, Degradation of lithium ion batteries employing graphite negatives and nickel–cobalt–manganese oxide + spinel manganese oxide positives: Part 2, chemical–mechanical degradation model, J. Power Sources 272 (2014) 1154–1161, http://dx.doi.org/10.1016/J.JPOWSOUR.2014.07.028.

[38] J.M. Reniers, D.A. Howey, Digital twin of a MWh-scale grid battery system for efficiency and degradation analysis, Appl. Energy 336 (2023) 120774, http://dx.doi.org/10.1016/J.APENERGY.2023.120774, URL https://linkinghub.elsevier.com/retrieve/pii/S0306261923001381.

[39] J.M. Reniers, G. Mulder, D.A. Howey, Unlocking extra value from grid batteries using advanced models, J. Power Sources 487 (December 2020) (2021) 229355, http://dx.doi.org/10.1016/j.jpowsour.2020.229355, URL https://linkinghub.elsevier.com/retrieve/pii/S0378775320316438.

[40] Y. Li, T. Wik, Y. Huang, C. Zou, Nonlinear model inversion-based output tracking control for battery fast charging, IEEE Trans. Control Syst. Technol. 32 (1) (2024) 225–240, http://dx.doi.org/10.1109/TCST.2023.3306240, URL https://ieeexplore.ieee.org/document/10234584/.

[41] G. Ceusters, M.A. Putratama, R. Franke, A. Nowé, M. Messagie, An adaptive safety layer with hard constraints for safe reinforcement learning in multi-energy management systems, Sustain. Energy, Grids Netw. 36 (2023) 101202, http://dx.doi.org/10.1016/j.segan.2023.101202, URL https://linkinghub.elsevier.com/retrieve/pii/S2352467723002102.

[42] J.M. Reniers, G. Mulder, S. Ober-Blöbaum, D.A. Howey, Improving optimal control of grid-connected lithium-ion batteries through more accurate battery and degradation modelling, J. Power Sources 379 (September 2017) (2018) 91–102, http://dx.doi.org/10.1016/j.jpowsour.2018.01.004, URL https://linkinghub.elsevier.com/retrieve/pii/S0378775318300041.

[43] X. Dorronsoro, R. de Castro, J. Varela Barreras, E. Garayalde, U. Iraola, Battery aging-aware adaptive model predictive control based on coupled semi-empirical electro-thermal and aging models, Appl. Energy 401 (2025) 126494, http://dx.doi.org/10.1016/J.APENERGY.2025.126494, URL https://www-sciencedirect-com.tudelft.idm.oclc.org/science/article/pii/S0306261925012243?getft_integrator=scopus&pes=vor&utm_source=scopus#fd0080.

[44] J. Park, T. Kwon, M.K. Sim, Optimal energy storage system control using a Markovian degradation model—Reinforcement learning approach, J. Energy Storage 71 (2023) 107964, http://dx.doi.org/10.1016/j.est.2023.107964, URL https://www-sciencedirect-com.tudelft.idm.oclc.org/science/article/pii/S2352152X23013610#sec3.

[45] W. Powell, Reinforcement Learning and Stochastic Optimization: A Unified Framework for Sequential Decisions, vol. 22, Wiley, 2022, http://dx.doi.org/10.1080/14697688.2022.2135456, URL https://www.tandfonline.com/doi/full/10.1080/14697688.2022.2135456.

[46] L. Grüne, J. Pannek, Nonlinear Model Predictive Control Theory and Algorithms, Springer, 2017, http://dx.doi.org/10.1007/978-3-319-46024-6, URL URL http://www.springer.com/series/61.

[47] D. Slaifstein, G.R. Chandra Mouli, L. Ramirez-Elizondo, P. Bauer, Sequential operation of residential energy hubs using physics-based economic nonlinear MPC, Appl. Energy 408 (2026) 127402, http://dx.doi.org/10.1016/J.APENERGY.2026.127402, URL https://linkinghub.elsevier.com/retrieve/pii/S0306261926000541.

[48] N. Damianakis, G.C.R. Mouli, P. Bauer, Risk-averse estimation of electric heat pump power consumption, in: 2023 IEEE 17th International Conference on Compatibility, Power Electronics and Power Engineering (CPE-POWERENG), IEEE, 2023, pp. 1–6, http://dx.doi.org/10.1109/CPE-POWERENG58103.2023.10227424, URL https://ieeexplore.ieee.org/document/10227424/.

[49] Y. Cao, S.B. Lee, V.R. Subramanian, V.M. Zavala, Multiscale model predictive control of battery systems for frequency regulation markets using physics-based models, J. Process Control 90 (2020) 46–55, http://dx.doi.org/10.1016/J.JPROCONT.2020.04.001.

[50] H. Movahedi, S. Pannala, J. Siegel, S.J. Harris, D. Howey, A. Stefanopoulou, Extra throughput versus days lost in V2G services: Influence of dominant degradation mechanism, J. Energy Storage 104 (2024) 114242, http://dx.doi.org/10.1016/J.EST.2024.114242, URL https://linkinghub.elsevier.com/retrieve/pii/S2352152X24038283.

[51] E. Prat, R.M. Lusby, J.M. Morales, S. Pineda, P. Pinson, How long is long enough? finite-horizon approximation of energy storage scheduling problems, 2024, arXiv http://arxiv.org/abs/2411.17463.

[52] D. Slaifstein, J. Alpízar-Castillo, A. Menendez Agudin, Laura Ramírez-Elizondo, G. Ram Chandra Mouli, P. Bauer, Aging-aware Battery Operation for Multicarrier Energy Systems, in: 49th Annual Conference of the IEEE Industrial Electronics Society, IES, Singapore, 2023.

[53] Home - elaad nl, 2024, URL https://platform.elaad.io/.

[54] B. Planden, K. Lukow, P. Henshall, G. Collier, D. Morrey, A computationally informed realisation algorithm for lithium-ion batteries implemented with LiiBRA.jl, J. Energy Storage 55 (2022) 105637, http://dx.doi.org/10.1016/j.est.2022.105637, URL https://linkinghub.elsevier.com/retrieve/pii/S2352152X22016255.

[55] A. Rodríguez, G.L. Plett, M.S. Trimboli, Comparing four model-order reduction techniques, applied to lithium-ion battery-cell internal electrochemical transfer functions, ETransportation 1 (2019) http://dx.doi.org/10.1016/j.etran.2019.100009, URL https://linkinghub.elsevier.com/retrieve/pii/S2590116819300098.

[56] G.L. Plett, M.S. Trimboli, Battery Management Systems. Volume III : Physics-Based Methods, first ed., Artech House, Norwood, 2024, URL https://uk.artechhouse.com/Battery-Management-Systems-Volume-III-Physics-Based-Methods-P2201.aspx.

[57] G. Fan, D. Lu, M.S. Trimboli, G.L. Plett, C. Zhu, X. Zhang, Nondestructive diagnostics and quantification of battery aging under different degradation paths, J. Power Sources 557 (2023) 232555, http://dx.doi.org/10.1016/j.jpowsour.2022.232555, URL https://linkinghub.elsevier.com/retrieve/pii/S0378775322015324.

[58] The green village and fieldlab voor duurzame innovatie, 2024, URL https://www.thegreenvillage.org/.

[59] A. Smets, K. Jäger, O. Isabella, R. van Swaaij, M. Zeman, Solar Energy: The Physics and Engineering of Photovoltaic Conversion, Technologies and Systems, UIT Cambridge Ltd, 2016, URL https://ebookcentral-proquest-com.tudelft.idm.oclc.org/lib/delft/detail.action?docID=4781743.

[60] I. Diab, A. Saffirio, G.R. Chandra-Mouli, P. Bauer, A simple method for sizing and estimating the performance of PV systems in trolleybus grids, J. Clean. Prod. 384 (2023) 135623, http://dx.doi.org/10.1016/J.JCLEPRO.2022.135623.

[61] Epex spot - market data services, 2023, URL https://www.epexspot.com/en/marketdataservices.

[62] V. Sulzer, S.G. Marquis, R. Timms, M. Robinson, S.J. Chapman, Python battery mathematical modelling (PyBaMM), J. Open Res. Softw. 9 (1) (2021) 1–8, http://dx.doi.org/10.5334/JORS.309.

[63] G.L. Plett, Extended Kalman filtering for battery management systems of LiPB-based HEV battery packs: Part 2 modeling and identification, J. Power Sources 134 (2) (2004) 262–276, http://dx.doi.org/10.1016/J.JPOWSOUR.2004.02.032.

[64] J. Bezanson, A. Edelman, S. Karpinski, V.B. Shah, Julia: A fresh approach to numerical computing, SIAM Rev. 59 (1) (2017) 65–98, http://dx.doi.org/10.1137/141000671.

[65] M. Lubin, O. Dowson, J.D. Garcia, J. Huchette, B. Legat, J.P. Vielma, JuMP 1.0: Recent improvements to a modeling language for mathematical optimization, 2022, arXiv http://arxiv.org/abs/2206.03866.

[66] J.L. Pulsipher, W. Zhang, T.J. Hongisto, V.M. Zavala, A unifying modeling abstraction for infinite-dimensional optimization, Comput. Chem. Eng. 156 (2022) 107567, http://dx.doi.org/10.1016/j.compchemeng.2021.107567.

[67] R.H. Byrd, J. Nocedal, R.A. Waltz, Knitro: An Integrated Package for Nonlinear Optimization, Springer, Boston, MA, 2006, http://dx.doi.org/10.1007/0-387-30065-1_4, URL http://link.springer.com/10.1007/0-387-30065-1_4.

[68] S. Boyd, Convex Optimization, Cambridge University Press, New York, NY, USA, 2011, http://dx.doi.org/10.1145/2020408.2020410, URL https://dl.acm.org/doi/10.1145/2020408.2020410.

[69] G. Darivianakis, A. Eichler, R.S. Smith, J. Lygeros, A data-driven stochastic optimization approach to the seasonal storage energy management, IEEE Control. Syst. Lett. 1 (2) (2017) 394–399, http://dx.doi.org/10.1109/LCSYS.2017.2714426, URL http://ieeexplore.ieee.org/document/7945264/.

[70] L.D. Couto, J. Reniers, D. Zhang, D.A. Howey, M. Kinnaert, Degradation monitoring and characterization in lithium-ion batteries via the asymptotic local approach, IEEE Trans. Control Syst. Technol. 33 (1) (2025) 189–206, http://dx.doi.org/10.1109/TCST.2024.3483093, URL https://ieeexplore-ieee-org.tudelft.idm.oclc.org/document/10754953.

[71] J. Reniers, Degradation-aware Optimal Control of Grid-Connected Lithium-Ion Batteries, (Ph. D. thesis), University of Oxford, 2020.